

# Adiabatic dynamics of coupled spins and phonons in magnetic insulators

Shang Ren,<sup>1,2</sup> John Bonini,<sup>2</sup> Massimiliano Stengel,<sup>3,4</sup> Cyrus E. Dreyer,<sup>5,2</sup> and David Vanderbilt<sup>1</sup>

<sup>1</sup>*Department of Physics and Astronomy, Rutgers University, Piscataway, New Jersey 08854, USA*

<sup>2</sup>*Center for Computational Quantum Physics, Flatiron Institute,  
162 5th Avenue, New York, New York 10010, USA*

<sup>3</sup>*Institut de Ciència de Materials de Barcelona (ICMAB-CSIC), Campus UAB, 08193 Bellaterra, Spain*

<sup>4</sup>*ICREA-Institució Catalana de Recerca i Estudis Avançats, 08010 Barcelona, Spain*

<sup>5</sup>*Department of Physics and Astronomy, Stony Brook University, Stony Brook, New York, 11794-3800, USA*

In conventional *ab initio* methodologies, phonons are calculated by solving equations of motion involving static interatomic force constants and atomic masses. The Born-Oppenheimer approximation, where all electronic degrees of freedom are assumed to adiabatically follow the nuclear dynamics, is also adopted. This approach does not fully account for the effects of broken time-reversal symmetry in systems with magnetic order. Recent attempts to rectify this involve the inclusion of the velocity dependence of the interatomic forces in the equations of motion, which accounts for time-reversal symmetry breaking, and can result in chiral phonon modes with non-zero angular momentum even at the zone center. However, since the energy ranges of phonons and magnons typically overlap, the spins cannot be treated as adiabatically following the lattice degrees of freedom. Instead, phonon and spins must be treated on a similar footing. Focusing on zone-center modes, we propose a method involving Hessian matrices and Berry curvature tensors in terms of both phonon and spin degrees of freedom, and describe a first-principles methodology for calculating these. We then solve Lagrange's equations of motion to determine the energies and characters of the mixed excitations, allowing us to quantify, for example, the energy splittings between chiral pairs of phonons in some cases, and the degree of magnetically induced mixing between infrared and Raman modes in others. The approach is general, and can be applied to determine the adiabatic dynamics of any mixed set of slow variables.

## I. INTRODUCTION

An outstanding challenge of first-principles materials theory is the development of a systematic treatment of the coupled dynamics of phonons and magnons in magnetic materials. The calculation of phonon dispersions has long been a standard feature of modern density-functional theory (DFT) codes, based either on finite-difference or linear-response calculations of the dynamical matrix [1–5]. On the other hand, magnon dispersions are most often computed in the context of discrete spin models, sometimes using parameters derived from DFT [6–9], although treatments based on time-dependent DFT (TDDFT) [10–17] and many-body perturbation theory [18–22] have also appeared. However, the consistent treatment of phonon and magnon dynamics on a similar footing, and the coupling between them, remains daunting [23].

Phonons play a crucial role in determining various thermodynamic and electronic properties of materials, including heat capacity, heat transport, electronic conductivity, and superconductivity. Conventionally, phonons are treated within the Born-Oppenheimer approximation [24], i.e., assuming that the electronic degrees of freedom (DOF) can adiabatically follow the motion of the atoms. In these calculations, the potential energy in the phonon Hamiltonian is computed as a function of atomic displacements. The usual harmonic approximation involves keeping only the leading quadratic dependence of the energy on displacement, encoded in the interatomic force constant (IFC) matrix, i.e., the Hes-

sian matrix of the energy. Anharmonic treatments go further by taking account of higher-order tensors which describe third and higher derivatives with respect to displacements. These harmonic and anharmonic tensors are all invariant under time-reversal symmetry (TRS), so that at this level of description the phonons are assumed to preserve TRS and to possess the symmetries of the nonmagnetic group.

However, this assumption is incorrect for materials with magnetic order or in the presence of an external magnetic field. Recent efforts have been made to address this issue by incorporating the nuclear Berry potential into the effective Hamiltonian [25–33], which arises naturally when the electronic DOF are integrated out under the Born-Oppenheimer approximation, as first pointed out by Mead and Truhlar [25]. The nuclear Berry potential introduces a velocity-dependent force into the equations of motion (EOM), which is determined by the nuclear Berry curvature multiplied by the nuclear velocity.

Theoretical studies have made several predictions regarding the impact of the nuclear Berry curvature on zone-center chiral phonons [26–29, 31–33], and their contribution to the thermal Hall effect [34–37]. Experimental evidence has also emerged supporting the existence of zone-center chiral phonons [38, 39] and the phonon thermal Hall effect [40, 41]. We define chiral phonons as those that respect rotational symmetry but possess complex eigenvalues under the rotation operator. Chiral phonons have attracted attention due to their unique properties, such as their selective excitation by circular-polarized light with different helicities [38, 39, 42, 43], their coupling to electronic states with distinct chirality

ties [44] following the selection rule proposed in Ref. [45], and their ability to demonstrate Floquet behavior when driven by lasers [46]. Additionally, chiral phonons can possess phonon magnetic moments [47–49].

To date, much of the theoretical literature treats models in which the nuclear Berry curvature is an adjustable parameter. The first-principles calculation of the nuclear Berry curvature is still in its infancy, with only a few calculations for molecular [30] and crystalline [33] systems.

Spin-wave excitations, or magnons, constitute additional DOF in magnetic materials. These excitations are chiral from the outset; for example, in the presence of easy-axis anisotropy, spins always precess clock-wise when viewed end-on. While it is not so widely appreciated, magnon dynamics can also be formulated and computed in the context of a geometric-phase framework [50, 51]. There is no inertial term in the spin dynamics, but the Berry curvature tensor enters the EOM by describing the spin precession in response to a torque [52]. This raises the possibility of a uniform treatment of both nuclear and spin degrees of freedom in a common theoretical framework.

Crucially, the frequency (or energy) range of the magnons strongly overlaps that of the phonons. In metals these also overlap with electron-hole excitations, but we shall restrict our attention here to insulators in which there is a clear energy separation between both phonons and magnons on the one hand, and cross-gap electronic excitations on the other. In this case, both types of bosonic excitations can be treated as “slow” DOF, with the remainder of the electronic system following adiabatically. In such cases it is crucial to treat both phonon and spin DOF on the same footing.

A first step was taken in this direction in Ref. [33] for the case of bulk ferromagnetic  $\text{CrI}_3$ . In that work, a minimal model was proposed in which the nuclear Berry curvature arose entirely from the canting of Cr spins in response to atomic displacement. Though this model captured the essential physics of  $\text{CrI}_3$ , a general and quantitatively accurate theory should include other contributions to the Berry curvature including “phonon-only” Berry curvature arising from atomic displacements at fixed spin, and mixed “spin-phonon” Berry curvature. Such contributions can play an important role, particularly in predicting energy splittings of high-energy chiral phonons. Additionally, Ref. [33] relied on the input of experimental magnon energies, which may not always be available.

Motivated by the need for better fundamental and quantitative understanding of phonons in TRS-broken systems, we present a generalized adiabatic treatment incorporating all relevant Hessian matrices and Berry curvatures for both phonons and spins. It should be noted that the methodology presented in this work provides a general theoretical framework for treating dynamics beyond the specific case of coupled spins and phonons. I.e., it allows for efficient *ab initio* calculation of the adiabatic dynamics of any mixed set of slow variables.

This goes significantly beyond the more approximate approach of Ref. [33], which we shall refer to as the minimal spin-phonon model below. We also demonstrate an *ab initio* methodology to calculate these matrices. We conduct four case studies covering ferromagnetic (FM) and antiferromagnetic (AFM) materials in both three-dimensional (3D) and two-dimensional (2D) form. We investigate the energy splittings and symmetries of chiral phonons in these systems.

We show that, interestingly, circularly polarized chiral phonons do not always exhibit energy splittings when TRS is broken; whether this splitting occurs depends on the point group symmetry in the presence of magnetic order. Also, terms beyond the IFC are needed to correctly capture the symmetry of phonons in cases where magnetic order breaks a spatial symmetry  $g$ , but the combination of  $g$  and time reversal  $\mathcal{T}$  remains a symmetry. This limitation arises because conventional phonon calculations rely on real-symmetric IFC and atomic mass matrices that preserve TRS.<sup>1</sup> We show that correct accounting for phonon symmetries is crucial for determining Raman/IR activities.

This paper is organized as follows. In Sec. II, we establish the theoretical framework via the Lagrangian formalism of adiabatic dynamics, and derive EOM that treat spins and phonons on an equal footing. We also revisit phonon angular momentum and introduce the concept of atom-resolved phonon angular momentum. Section III details the proposed method for calculating all the matrices involved in the present approach, along with the computational details. In Sec. IV, we present our results, which include the analysis of phonons and magnons in 3D FM  $\text{CrI}_3$  bulk (Sec. IV A), 3D AFM  $\text{Cr}_2\text{O}_3$  bulk (Sec. IV B), and 2D systems (Sec. IV C) such as FM  $\text{CrI}_3$  monolayer (Sec. IV C 1) and AFM  $\text{VPSe}_3$  monolayer (Sec. IV C 2). Section V provides a discussion of the role of spin-orbit coupling (Sec. V A) and future experimental investigations (Sec. V B). Finally, we summarize our findings and present concluding remarks in Sec. VI.

## II. THEORETICAL BACKGROUND

We restrict our considerations to the case of insulating magnetic materials in which there is a clear separation between the energy scales of the phonons and the cross-gap electronic excitations. The magnetic order insures that there will also be dynamics associated with spin fluctuations, i.e., the magnons. If the magnon frequencies would be higher than, and robustly gapped from, those of the phonons, it would be possible to treat all electronic

---

<sup>1</sup> If  $g$  is a symmetry of the nonmagnetic crystal, but neither  $g$  nor  $g\mathcal{T}$  remains a symmetry in the presence of magnetic order, the symmetry breaking of  $g$  will still manifest itself in the real IFC matrix.

excitations, including the magnons, as adiabatically following the phonon DOF. However, this is almost never the case. In the present work, we therefore treat both the lattice and spin DOF on a similar footing, while assuming that there is still a large energy gap between the top of the phonon or magnon spectrum and the onset of cross-gap electronic excitations.

We formulate our theory in the context of a first-principles mean-field theory such as DFT, where the dynamics of the nuclei is treated classically while the electronic system is evolved according to the time-dependent Schrödinger equation. This is essentially the domain of time-dependent DFT (TDDFT), but here we aim to treat the spin DOF as slow semiclassical variables alongside the nuclear displacements. This requires a separation of the electronic DOF into a small number of spin DOF and the remaining large number of electronic excitations on the scale of the band gap or above.

To do so, we define a “spin” unit vector on a magnetic ion to be the direction of the average spin density inside a Wigner-Seitz sphere centered at that site, and subsequent calculations of electronic ground states and energies are always computed with these spin variables constrained. The essential requirement is that the remaining electronic system, so constrained, should be free of any remaining slow DOF, i.e., any below-band-gap excitations. The implementation of the Wigner-Seitz sphere constraint is not a serious obstacle in practice, as most DFT code packages have features for carrying out electronic minimizations under the constraint of fixed spin orientations defined in this way. We emphasize that we treat not only the lattice displacements, but also the spin cantings, in a harmonic approximation about the ground-state reference structure. We treat only collinear easy-axis systems here, and assume that the spin cantings with respect to this axis are small.

To finish a discussion of the approximations of our theory, we note that we use “ordinary” adiabatic dynamics, in which the adiabatic perturbation theory is carried only to first order in the rate of change of nuclear or spin variables. This is well justified as long as the gap separating phonons and magnons from interband electronic excitations is large. And finally, we shall shortly make a harmonic approximation, in which the atomic displacements and spin cantings are expanded to leading order around a ground-state reference configuration.

With these understandings, we turn now to a detailed presentation of our methodology.

### A. Lagrangian formulation of adiabatic dynamics

While the Hamiltonian formalism is commonly used in the literature to analyze chiral phonons [25, 26, 30, 31, 33], we will instead start with the Lagrangian formalism. We show in Sec. II C that this approach is well-suited to developing a comprehensive model of the coupled spin-phonon dynamics, while avoiding the difficulties associ-

ated with defining canonical momentum for spins. The Lagrangian takes the form

$$L = \frac{1}{2} \sum_i M_i \dot{Q}_i^2 - \epsilon(Q) + \hbar \sum_i \dot{Q}_i A_i, \quad (1)$$

where the configuration  $Q$  can represent any slow variables. While the formulation is general, we shall focus on the case that  $Q$  represents both the nuclear coordinates and the spin variables, where the latter act as constraints on the spin moments as explained above. For clarity of presentation, we assume a finite number of nuclear and spin DOF, as for a molecule or the  $\Gamma$ -point modes of a periodic crystal.

The first term in Eq. (1) is the kinetic energy associated with the  $i$ -th degree of freedom, where  $M_i$  is the nuclear mass for the phonon variables or zero for the spin-canting variables. The second term is the potential energy, and the third represents the coupling between the time derivative of the adiabatic variable  $Q_i$  and the Berry potential  $A_i$  [50]. The latter is defined as

$$A_i(Q) = \langle \psi(Q) | i \frac{\partial}{\partial Q_i} | \psi(Q) \rangle, \quad (2)$$

where  $|\psi(Q)\rangle$  represents the electronic wave function at constrained nuclear coordinates and spin orientations  $Q$ .

By solving the Euler-Lagrangian equation for the Lagrangian defined in Eq. (1), we obtain

$$M_i \ddot{Q}_i + \hbar \dot{A}_i = -\partial_i \epsilon(Q) + \hbar \sum_j \dot{Q}_j \partial_i A_j, \quad (3)$$

where  $\partial_i$  denotes  $\partial/\partial Q_i$ . By using  $\dot{A}_i = \sum_j \partial_j A_i \dot{Q}_j$ , we can simplify Eq. (3) to

$$\begin{aligned} M_i \ddot{Q}_i &= -\partial_i \epsilon(Q) + \hbar \sum_j \dot{Q}_j (\partial_i A_j - \partial_j A_i), \\ &= -\partial_i \epsilon(Q) + \sum_j G_{ij}(Q) \dot{Q}_j. \end{aligned} \quad (4)$$

Here

$$G_{ij}(Q) = \hbar \Omega_{ij}(Q) = \hbar (\partial_i A_j - \partial_j A_i), \quad (5)$$

where  $\Omega_{ij}$  is the Berry curvature, and is therefore gauge-invariant. Although the gauge-dependent quantity  $A_i(Q)$  appears in the Lagrangian, the EOM are gauge-invariant since only  $G_{ij}(Q)$  appears.

In this work, we focus on small oscillations near equilibrium. To simplify the analysis, we introduce the generalized displacement vector  $q$  defined via  $Q_i = Q_i^{(0)} + q_i$ , where  $Q_i^{(0)}$  is the equilibrium value of the  $i$ -th degree of freedom. Introducing the harmonic approximation, we expand the potential energy  $\epsilon(Q)$  in terms of  $q$  as

$$\epsilon(Q) = \epsilon(Q_0) + \frac{1}{2} \sum_{ij} K_{ij} q_i q_j + \dots, \quad (6)$$

where  $K_{ij}$  is the Hessian matrix in  $q_i$  and  $q_j$ , i.e.,  $K_{ij} = \partial_i \partial_j \epsilon(Q)|_{Q=Q_0}$ . The EOM for  $q$  is then given by

$$M_i \ddot{q}_i = - \sum_j K_{ij} q_j + \sum_j G_{ij} \dot{q}_j, \quad (7)$$

where  $G = G(Q)|_{Q=Q_0}$  is also computed at the reference configuration  $Q_0$ . Conventional treatments of phonons in isolation typically use only mass and force-constant matrices  $M$  and  $K$ , while spin dynamics in isolation is described by the anisotropy tensor  $K$  and Berry curvature  $G$ . Note that  $M$  is real diagonal,  $K$  is real symmetric, and  $G$  is real antisymmetric.

To determine the frequencies, we substitute  $q_i(t) = e^{-i\omega t} q_i$  into Eq. (7), yielding

$$-\omega_n^2 M |q_n\rangle = -K |q_n\rangle - i\omega_n G |q_n\rangle, \quad (8)$$

where  $|q_n\rangle$  is a column vector with the  $i$ -th component  $q_{n,i}$  corresponding to the  $n$ -th mode associated with DOF  $i$ . Equation (8) is easily solved using, e.g., the methods of Sec. III C. The above treatment provides a semiclassical theory of the adiabatic dynamics of the system.

### B. Mead-Truhlar approach without explicit spin degrees of freedom

If we limit the slow variables  $Q$  to include only atomic coordinates, i.e., allowing all electronic degrees of freedom (including spins) to be in their instantaneous ground state for a given  $Q$ , we restore the treatment of Mead and Truhlar in Ref. [25]. To indicate the specialization to atomic coordinates, in this section we replace  $Q$  and  $q$  by  $R$  and  $u$ , where  $R$  denotes the equilibrium position for atomic coordinates, and  $u$  denotes the atomic displacement from the equilibrium. Now the EOM for  $u$  in the harmonic approximation is

$$M_l^{\text{MT}} \ddot{u}_l = - \sum_n K_{lm}^{\text{MT}} u_m + \sum_n G_{lm}^{\text{MT}} \dot{u}_m, \quad (9)$$

where  $l$  and  $m$  are composite indices for  $I\alpha$ ,  $I$  runs over atoms and  $\alpha$  represents a Cartesian direction. Equation (9) shows that  $G_{mn}^{\text{MT}} \dot{u}_n$  corresponds to a force acting on coordinate  $m$  that is proportional to the velocity of coordinate  $n$ . An alternative derivation of Eq. (9) using the quantum theory in the Hamiltonian framework is given in Appendix A.

The conventional treatment of phonons [1, 2] is recovered by discarding the term involving the nuclear Berry curvature  $G^{\text{MT}}$  in Eq. (9). This is justified in TR-invariant systems, where  $G^{\text{MT}}$  vanishes by symmetry. However,  $G^{\text{MT}}$  is often neglected even when the system is not TR symmetric, with the consequences that Eq. (9) obeys TRS and the phonons will not have the correct symmetry of the TRS-broken system. This will force modes with opposite chirality to be degenerate at the zone center, which is not necessarily the case in a magnetic material.

Recent works have used Eq. (9) to demonstrate splitting of chiral modes as a result of TRS breaking [31, 33]. However, it was demonstrated in Ref. [33] that for  $\text{CrI}_3$ , the main contribution to  $G^{\text{MT}}$  comes from canting and precession of spins. As mentioned earlier, the energy scale for spin rotations corresponds to the frequency of the magnons, which is close to that of the phonons in most systems. Consequently, the assumption that atomic displacements are the only slow DOF in the system, which led to Eq. (9), is not valid. Reference [33] developed a Hamiltonian formalism for coupled spin-phonon dynamics that we refer to here as the ‘‘minimal spin-phonon model.’’ In the next section we will develop a more general Lagrangian-based approach that is well suited to treating phonon and spin dynamics together.

### C. Treatment of spins and phonons on the same footing

We now return to the framework of Eq. (7) in which  $q_i$  includes both nuclear and spin DOF. The Euler-Lagrange EOM derived from Eq. (7) is

$$\sum_j M_{ij} \ddot{q}_j = - \sum_j K_{ij} q_j + G_{ij} \dot{q}_j, \quad (10)$$

where  $i$  runs over both phonon and spin DOF. In the phonon sector,  $q_i = u_{I\alpha}$  is a shorthand for a small displacement of atom  $I$  in Cartesian direction  $\alpha = \{x, y, z\}$ . In the spin sector,  $q_i$  denotes a small spin canting  $q_i = s_{J\beta}$ , where  $J$  runs only over magnetic ions and  $\beta$  indexes the spin canting in the two directions orthogonal to the ground-state spin orientation. Specializing to easy-axis systems with spin axis along  $\pm\hat{z}$ , we let  $\beta$  run over only the two in-plane Cartesian directions. That is,  $q_i = s_{J\beta} = S_{J\beta}/|S_J|$  describes the component  $\beta = \{x, y\}$  of the unit vector of spin  $S_J$  located on the  $J$ -th magnetic ion.

The matrix  $M_{ij}$  in Eq. (10) is the diagonal mass matrix introduced in Eq. (1), with zero entries for the spin DOF;  $K_{ij} = \partial_i \partial_j \epsilon(\mathbf{q})$  is a generalized Hessian matrix; and  $G_{ij} = \hbar \Omega_{ij} = \hbar(\partial_i A_j - \partial_j A_i)$  embodies the Berry curvature as in Eq. (5). In these last two expressions,  $\partial_j$  denotes  $\partial/\partial q_j$ , which can be a derivative with respect to either nuclear or spin-canting coordinates, evaluated at the reference ground-state configuration. It should be emphasized that in our formulation, the Hessian matrices are expanded to quadratic order in phonon or magnon amplitudes, resulting in a harmonic theory with infinite lifetimes for both phonons and magnons. This is also evident in the hermiticity of Eq. (10). While including anharmonic interactions beyond quadratic order would allow decay of a phonon or magnon excitation into two or more lower-energy excitations, thereby rendering their lifetimes finite, such effects are not considered in this work and remain an area for future investigation.

In this context, derivatives with respect to nuclear coordinates must be taken at fixed spin. That is, the ma-



trices  $K$  and  $G$  are now computed in terms of the electronic quantum state  $|\psi(R, s)\rangle$ , rather than  $|\psi(R)\rangle$  as in Sec. II B. As explained earlier, this requires a calculation of the electronic ground state subject to constrained spin orientations. While there is some freedom in the definition of the spin unit vector, we follow the established approach of defining it in terms of the integrated spin density inside a Wigner-Seitz sphere, as discussed in Sec. III B. This choice encodes the distinction between “spin” and “other electronic” DOF in our theory.

To simplify the analysis, we can partition all DOF  $i$  into phonon DOF (labeled as p) and spin DOF (labeled as s). The matrices in Eq. (10) can then be represented using a block structure as

$$\begin{aligned} M &= \begin{pmatrix} M^{(\text{pp})} & 0 \\ 0 & 0 \end{pmatrix}, \\ K &= \begin{pmatrix} K^{(\text{pp})} & K^{(\text{ps})} \\ K^{(\text{sp})} & K^{(\text{ss})} \end{pmatrix}, \\ G &= \begin{pmatrix} G^{(\text{pp})} & G^{(\text{ps})} \\ G^{(\text{sp})} & G^{(\text{ss})} \end{pmatrix}. \end{aligned} \quad (11)$$

We use the term “bare phonons” to refer to phonons that are calculated without considering  $G^{(\text{pp})}$ ,  $G^{(\text{ps})}$  ( $G^{(\text{sp})}$ ), or  $K^{(\text{ps})}$  ( $K^{(\text{sp})}$ ), while phonons calculated with the inclusion of those terms are referred to as “perturbed phonons.” The term “perturbed” is used in recognition of the fact that the influence of these terms is generally small, although we solve Eq. (10) exactly. Nevertheless, we also provide a perturbation analysis of  $K^{(\text{sp})}$ ,  $G^{(\text{sp})}$ , and  $G^{(\text{pp})}$  in Appendix D, illuminating the physical implications of each term, and thereby offering valuable insight.

It is worth noting that  $G^{(\text{pp})}$ ,  $G^{(\text{ps})}$  ( $G^{(\text{sp})}$ ), and  $K^{(\text{ps})}$  ( $K^{(\text{sp})}$ ) are zero in the absence of spin-orbit coupling (SOC) in collinear systems, a point elaborated upon in Sec. V A below. In that case, the broken TRS in the spin sector is never communicated to the orbital electronic sector or, in turn, to the phonon sector.

Importantly, in the case that  $K^{(\text{ps})}$  ( $K^{(\text{sp})}$ ) and  $G^{(\text{ps})}$  ( $G^{(\text{sp})}$ ) vanish, phonons and spins decouple, and Eq. (10) reduces to the EOM for phonons and magnons separately. In the phonon sector, it reduces to Eq. (9) which corresponds to the approach proposed by Mead and Truhlar [25]. Meanwhile, in the magnon sector, it reduces to

$$\hbar\Omega^{(\text{ss})}|\dot{s}\rangle = K^{(\text{ss})}|s\rangle, \quad (12)$$

which aligns with the EOM for magnons presented in Ref. [50]. Additionally, when  $\Omega^{(\text{ss})}$  is simplified to consider only isolated spinors, rendering inter-spin elements negligible, Eq. (12) reduces to the well-known Landau-Lifshitz equation [52, 53]. Further, if the energies of phonons are considerably lower than those of magnons, Eq. (10) in the phonon sector also reduces to the Mead-Truhlar approach, as discussed in Ref. [33].

The present approach defined by Eqs. (10) and (11) uses Hessian matrices and Berry curvature tensors in

terms of all DOF. In contrast, the minimal spin-phonon model presented in Ref. [33] included only the spin-spin component of the Berry curvature, so that  $G^{(\text{pp})}$ ,  $G^{(\text{ps})}$ , and  $G^{(\text{sp})}$  were assumed to vanish. Furthermore, the minimal spin-phonon model in Ref. [33] only includes one bare phonon doublet and one bare magnon. In Appendix B, we will discuss a more comprehensive version of the spin-phonon model which incorporates all bare phonons and magnons but still neglects  $G^{(\text{pp})}$ ,  $G^{(\text{ps})}$ , and  $G^{(\text{sp})}$ , and discuss its connection to the minimal spin-phonon model and its equivalence with the widely employed Landau-Lifshitz equation [52]. We demonstrate that our approach, through the inclusion of non-trivial  $\Omega^{(\text{pp})}$ ,  $K^{(\text{sp})}$ , and  $\Omega^{(\text{sp})}$  terms, provides a fruitful generalization of the Landau-Lifshitz equation.

#### D. Phonon angular momentum

Before discussing the first-principles methodology to calculate the terms in Eq. (10) and Eq. (11), we review the definition of phonon angular momentum and introduce the concept of atom-resolved phonon angular momentum, as this will be important for characterizing the chiral modes in Sec. IV. The definition of phonon angular momentum can be found in the literature [26], and we briefly revisit the relevant definitions here. First, we note that by solving Eq. (10), one can obtain an energy eigenvalue  $\omega_n$  and the corresponding mode with both phonon and spin components, i.e.,  $|q_n\rangle = |u_n\rangle \oplus |s_n\rangle$ , where  $n$  runs over different solutions of Eq. (10). Since we are mainly interested in the phonon sector in the present work, we define the atom-resolved phonon angular momentum using the phonon part  $|u_n\rangle$  of the mode.

The solutions to the EOM described by Eq. (10) yield energies that differ from those of the bare phonons. However, in all of the systems examined in this work, the differences between these energies and those of the bare phonons are relatively small. As such, we can identify the mode  $|q_n\rangle$  as “phonon-like” if its energy  $\omega_n$  is in close proximity to that of a bare phonon. Furthermore, we note that for a phonon-like mode  $|q_n\rangle$ , the  $|s_n\rangle$  contributions are very small compared to  $|u_n\rangle$ . In systems where the frequencies of the phonons and magnons coincide, the aforementioned conditions may not be met; nonetheless, in all cases we consider in this work, the zone-center phonons and magnons of relevance exhibit distinct energies, thus ensuring well-defined phonon-like and magnon-like modes.

For phonon-like modes, we continue to adopt the normalization convention

$$\langle u_n | M^{(\text{pp})} | u_n \rangle = 1, \quad (13)$$

even though  $\langle u_m | M^{(\text{pp})} | u_n \rangle$  is no longer exactly zero for  $m \neq n$ . It is also possible to have a “perturbed magnon” solution, which is a magnon-like solution with tiny phonon components.

The definition of phonon angular momentum was originally proposed in Ref. [26]. For a phonon-like mode  $|u_n\rangle$ , the atom-resolved phonon angular momentum (ARPAM)  $L_{n,Iz}$ , for atom  $I$  of mass  $M_I$  in the  $z$  direction is

$$\begin{aligned} L_{n,Iz} &= \hbar M_I (u_{n,Ix}^* u_{n,Iy}^*) \begin{pmatrix} 0 & -i \\ i & 0 \end{pmatrix} \begin{pmatrix} u_{n,Ix} \\ u_{n,Iy} \end{pmatrix} \\ &= 2\hbar M_I \text{Im}[u_{n,Ix}^* u_{n,Iy}], \end{aligned} \quad (14)$$

with  $L_{n,Ix}$  and  $L_{n,Iy}$  defined similarly by cyclic permutation of Cartesian indices. Note that if the projection of a mode vector on a given atom is of the form  $\hat{x} + i\hat{y}$ , the atom undergoes a counterclockwise rotation when viewed from above and contributes a positive  $L_z$ . The total phonon angular momentum (PAM)<sup>2</sup>  $L_{n,z}$  is defined as

$$L_{n,z} = \sum_I L_{n,Iz}, \quad (15)$$

which is the sum of the angular momenta  $L_{n,Iz}$  over all atoms  $I$ .

The bare phonons solve the secular equation involving only  $M^{(\text{pp})}$  and  $K^{(\text{pp})}$ , which is equivalent to the conventional phonon treatment of Eq. (9) with  $G = 0$ . These bare phonons can always be chosen real, in which case it follows from Eq. (14) that the full PAM and individual ARPAM always vanish. In the case of degenerate modes it may be possible to choose chiral linear combinations, but the trace over the degenerate set of modes always results in zero PAM and ARPAM. This is a consequence of the fact that TRS has not yet been broken at the bare level of description.

### III. METHODS

#### A. Finite difference method

This section demonstrates how to compute all matrices in Eq. (11) using finite-difference methods in the context of first-principles calculations. The nuclear masses  $M^{(\text{pp})}$  are trivially known. All calculations are carried out using the DFT methodology described in Sec. III B at fixed atomic coordinates and fixed spin orientations, where the latter are defined in terms of an integration of the spin density over a Wigner-Seitz sphere as mentioned earlier.

<sup>2</sup> We are aware that in some literature, the PAM is referred to as ‘‘pseudo angular momentum’’ [45], which is a non-zero integer multiple of  $\hbar$  if the phonon respects  $C_n$  symmetry with a nontrivial eigenvalue. However, it is important to note that the phonon angular momentum discussed in this paper is the kinetic angular momentum and is not conserved in the absence of infinitesimal rotational symmetry in the lattice. In contrast, the pseudo angular momentum is conserved up to  $n\hbar$  if the system possesses  $C_n$  symmetry. In Sec. IV, we refer to the  $C_3$  eigenvalue as  $\chi(C_3)$ .

The force-constant matrix  $K^{(\text{pp})}$ , which is also the Hessian matrix of the energy with respect to nuclear DOF, is defined as

$$K_{lm}^{(\text{pp})} = \frac{\partial^2 \epsilon}{\partial u_l \partial u_m} = -\frac{\partial F_l}{\partial u_m}. \quad (16)$$

Here  $l$  and  $m$  run over nuclear DOF and  $\epsilon$  is the total energy  $\epsilon(s, R)$  of the configuration  $s, R$ . The matrix element  $K_{lm}^{(\text{pp})}$  is computed by taking the finite difference of the Hellmann-Feynman forces  $F_l$  [1, 2] while constraining the spin directions to lie along  $\hat{z}$ .

The Hessian matrix of the energy with respect to spin DOF is denoted by  $K^{(\text{ss})}$ , with elements defined as

$$K_{ab}^{(\text{ss})} = \frac{\partial^2 \epsilon}{\partial s_a \partial s_b}, \quad (17)$$

where  $a$  and  $b$  run over spin DOF. To calculate  $K^{(\text{ss})}$ , we compute the second derivatives of the total energy with respect to small canting of the spins. Specifically, letting  $s_a = s_{I\alpha}$  and  $s_b = s_{J\beta}$ , for each pair  $(I, J)$  we compute the energies of  $(\alpha, \beta) = \pm(0.02, 0)$ ,  $\pm(0, 0.02)$ , and  $\pm(0.02, 0.02)$  relative to the ground state, while constraining all other spin moments to remain along  $\hat{z}$ .

The spin-phonon Hessian matrix  $K^{(\text{sp})}$  is defined as

$$K_{al}^{(\text{sp})} = \frac{\partial^2 \epsilon}{\partial s_a \partial u_l} = -\frac{\partial F_l}{\partial s_a}, \quad (18)$$

where  $a$  and  $l$  respectively run over the spin and nuclear DOF.  $K_{al}^{(\text{sp})}$  is computed by taking the finite-difference derivative of the force  $F_l$  with respect to the spin coordinate  $s_a$ .

An alternative approach to calculating  $K^{(\text{sp})}$  was described in Ref. [33]. Near the ground state, the energy  $\epsilon$  of the entire system can be expanded as

$$\epsilon = \frac{1}{2} \sum_{lm} K_{lm}^{(\text{pp})} u_l u_m + \sum_{al} K_{al}^{(\text{sp})} s_a u_l + \frac{1}{2} \sum_{ab} K_{ab}^{(\text{ss})} s_a s_b. \quad (19)$$

As  $\epsilon$  is minimized with  $s_a$ , we have

$$\frac{\partial \epsilon}{\partial s_a} = \sum_l K_{al}^{(\text{sp})} u_l + \sum_b K_{ab}^{(\text{ss})} s_b = 0. \quad (20)$$

We define a spin response matrix  $\chi^{(\text{sp})}$  as

$$\chi_{al}^{(\text{sp})} = \frac{\partial s_a}{\partial u_l} \simeq \frac{s_a}{u_l}, \quad (21)$$

where the second equality holds if both  $s_a$  and  $u_l$  are small. Then we can obtain

$$K^{(\text{sp})} = -K^{(\text{ss})} \chi^{(\text{sp})}, \quad (22)$$

where we have restored the matrix form for simplicity. In practice, one can perturb the ground state structure with  $u_l$  by manually moving the atoms from the equilibrium position and calculate the spin canting  $s_a$  with respect to

$u_l$ . We used Eq. (22) to calculate  $K^{(\text{sp})}$  for bulk  $\text{CrI}_3$ , and the result is consistent with Eq. (18). However, due to the slow convergence of spin relaxation, we recommend using Eq. (18) to calculate  $K^{(\text{sp})}$ .

In Eq. (11),  $G$  is simply  $\hbar$  times  $\Omega$ , where  $\Omega$  is the Berry curvature. The latter is computed using Stokes' theorem as expressed by

$$\Omega_{ij} = \frac{\Phi_{ij}}{2|\delta q_i \wedge \delta q_j|}, \quad (23)$$

where  $i$  and  $j$  run over all DOF, and  $\Phi_{ij}$  is the Berry phase around a diamond-shaped region of parameter space whose area appears in the denominator. Specifically for, e.g., a finite system with electronic ground state wave function  $|\psi\rangle$ ,

$$\Phi_{ij} = -\text{Im} \ln [\langle \psi(+\delta q_i) | \psi(+\delta q_j) \rangle \langle \psi(+\delta q_j) | \psi(-\delta q_i) \rangle \langle \psi(-\delta q_i) | \psi(-\delta q_j) \rangle \langle \psi(-\delta q_j) | \psi(+\delta q_i) \rangle]. \quad (24)$$

In an extended crystal with a single occupied band, one must sum over the Bloch wave vector  $k$  in the Brillouin zone to obtain  $\Phi_{ij} = N_k^{-1} \sum_k \Phi_{ij}^{(k)}$ , where  $\Phi_{ij}^{(k)}$  is defined as in Eq. (24) but with  $\psi$  replaced by the Bloch function  $\psi_k$ .  $\Phi_{ij}$  now has the interpretation of a Berry phase per unit cell, consistent with the interpretation of the Hessian  $K$  as an energy per unit cell. To extend  $\Phi_{ij}^{(k)}$  to the multiband case, we can replace the inner product of two Bloch states with the overlap matrix in the usual way [54] as

$$\Phi_{ij}^{(k)} = -\text{Im} \ln \det [M^k(+\delta q_i, +\delta q_j) M^k(+\delta q_j, -\delta q_i) M^k(-\delta q_i, -\delta q_j) M^k(-\delta q_j, +\delta q_i)]. \quad (25)$$

Here, the overlap matrices are defined as

$$M_{mn}^k(\delta q_i, \delta q_j) = \langle \psi_{mk}(q_i) | \psi_{nk}(q_j) \rangle, \quad (26)$$

where  $m$  and  $n$  are band indices. When computing the matrices, a finite difference of  $0.015 \text{ \AA}$  is used for the phonon DOF, and  $0.02$  is used for the spin DOF. We take care to choose these finite differences to ensure they remain within the linear regime. The numerical values of  $K^{(\text{ss})}$  and  $G^{(\text{ss})}$  for all four studied materials can be found in Appendix C.

## B. First principles calculations

In this section, we provide computational details for calculating matrices using the finite difference method described in Sec. III A. The reported DFT calculations are performed using the Vienna Ab-initio Simulation Package (VASP) [55–57], employing the local-density-approximation (LDA) exchange-correlation functional [58] and the projector-augmented wave [59]

method, with Cr  $3s^2 3p^6 3d^5 4s^1$ , I  $5s^2 5p^5$ , O  $2s^2 2p^4$ , V  $3s^2 3p^6 3d^5$ , P  $3s^2 3p^3$ , Se  $4s^2 4p^4$  pseudopotential valence configurations. A plane-wave cutoff of  $520 \text{ eV}$  is adopted for the  $\text{CrI}_3$  calculations, and  $500 \text{ eV}$  for the  $\text{Cr}_2\text{O}_3$  and  $\text{VPSe}_3$  systems.

All structures are relaxed using the local spin-density approximation (LSDA), and the convergence criteria for forces and energies are  $10^{-3} \text{ eV/\AA}$  and  $10^{-8} \text{ eV}$ , respectively. After relaxation, the wave functions are calculated using static calculations with a convergence criterion of  $10^{-10} \text{ eV}$  for energies. Spin-orbit coupling, which is essential to the physics described in this work, is included in all static calculations except structural relaxations.

We use  $\Gamma$ -centered Monkhorst-Pack  $k$ -points meshes [60] for all calculations, specifically  $5 \times 5 \times 5$  and  $7 \times 7 \times 7$  for bulk  $\text{CrI}_3$  and  $\text{Cr}_2\text{O}_3$  respectively, and  $7 \times 7 \times 1$  and  $6 \times 6 \times 1$  for monolayer  $\text{CrI}_3$  and  $\text{VPSe}_3$  respectively. For  $\text{Cr}_2\text{O}_3$  and  $\text{VPSe}_3$ , the Dudarev-type DFT+U approach [61] is used, with values of  $U=4.0 \text{ eV}$  and  $J=0.6 \text{ eV}$  for Cr and  $U=3.25 \text{ eV}$  and  $J=0$  for V (adapted from Refs. [62, 63]). For constrained local-moment calculations, the Wigner-Seitz radii for Cr and V are  $1.164$  and  $1.217 \text{ \AA}$ , respectively. The overlap matrix (Eq. (26)) is calculated as in Ref. [64]. Symmetry analysis is performed using the FINDSYM [65] and spglib [66] packages, while figures are rendered using VESTA [67].

## C. Solution of the equations of motion

In this section, we introduce a practical method for solving the EOM in Eq. (10). Given that the generalized mass matrix is non-invertible, conventional approaches are not directly applicable. We proceed as follows, although other potential methods may be suitable.

First, we rewrite Eq. (10) as

$$\frac{d}{dt} \begin{pmatrix} u \\ \dot{u} \\ s \end{pmatrix} = \begin{pmatrix} 0 & 1 & 0 \\ A_1 & A_2 & A_3 \\ B_1 & B_2 & B_3 \end{pmatrix} \begin{pmatrix} u \\ \dot{u} \\ s \end{pmatrix}, \quad (27)$$

which can be shown to reduce to Eq. (10) with the definitions

$$\begin{aligned} A_1 &= -[M^{(\text{pp})}]^{-1} K^{(\text{pp})} + [M^{(\text{pp})}]^{-1} G^{(\text{ps})} [G^{(\text{ss})}]^{-1} K^{(\text{sp})}, \\ A_2 &= [M^{(\text{pp})}]^{-1} G^{(\text{pp})} - [M^{(\text{pp})}]^{-1} G^{(\text{ps})} [G^{(\text{ss})}]^{-1} G^{(\text{sp})}, \\ A_3 &= -[M^{(\text{pp})}]^{-1} K^{(\text{ps})} + [M^{(\text{pp})}]^{-1} G^{(\text{ps})} [G^{(\text{ss})}]^{-1} K^{(\text{ss})}, \\ B_1 &= [G^{(\text{ss})}]^{-1} K^{(\text{sp})}, \\ B_2 &= -[G^{(\text{ss})}]^{-1} G^{(\text{sp})}, \\ B_3 &= [G^{(\text{ss})}]^{-1} K^{(\text{ss})}. \end{aligned} \quad (28)$$

The eigenvalues (multiplied by  $i$ ) of the matrix in Eq. (27), denoted as  $\omega_n$ , correspond to the solutions of Eq. (10). We restrict the index  $n$  to run only over solutions for which  $\omega_n > 0$ , which we take to be the physically meaningful ones.

In practice we find that small numerical errors remain in the eigenvectors, which arise from the fact that a Hermitian eigensolver cannot be applied in the context of Eq. (27). We have found that these errors can easily be removed by following with a second step in which we substitute the computed energies  $\omega_n$  back into Eq. (10) and then apply a Hermitian eigensolver to recalculate the eigenvectors.

#### IV. RESULTS

We conduct four case studies covering both FM and AFM systems, in both 3D and 2D. In Sec. IV A, we present the results obtained from our present approach for bulk CrI<sub>3</sub>, focusing on chiral phonons. The significance of the Berry curvatures neglected in Ref. [33], is discussed in Sec. IV A 1, while the relevant solutions for the magnons are discussed in Sec. IV A 2. Subsequently, in Sec. IV B, we investigate the phonons and magnons in bulk Cr<sub>2</sub>O<sub>3</sub> using the present approach. Shifting our focus to monolayer systems in Sec. IV C, we first consider 2D FM CrI<sub>3</sub> in Sec. IV C 1, and then 2D AFM VPSe<sub>3</sub> in Sec. IV C 2.

##### A. Chiral phonons in bulk ferromagnetic CrI<sub>3</sub>

CrI<sub>3</sub> is a hexagonal van der Waals material that exhibits FM order in both bulk and monolayer phases [68]. It is an insulator with inversion and three-fold rotational symmetry around the  $z$ -axis in both phases. The magnetic moments on the Cr ions do not break the inversion symmetry. The symmetries will be discussed in detail below.

The crystal structure of the bulk CrI<sub>3</sub> unit cell is depicted in Fig. 1. For bulk CrI<sub>3</sub>, the structural and magnetic symmetries are identical (space group  $R\bar{3}$ , point group  $S_6$ ), regardless of the presence of FM order. That is, the magnetic space group is of Type I (“colorless”), in which no symmetry operations involve TR [69]. Therefore, the zone-center phonons can be categorized into the irreducible representations (irreps) of the  $S_6$  point group as  $4E_g \oplus 4E_u \oplus 4A_g \oplus 4A_u$ . Among these, one  $A_u$  mode and one pair of  $E_u$  modes are acoustic modes. In this work, we will focus on the optical modes.

The  $E_g$  and  $E_u$  irreps are complex-conjugate irreps, which are more properly decomposed further into one-dimensional irreps of opposite chirality. In the presence of TRS, or when neglecting the term involving the Berry curvature  $G$  tensor in Eq. (9), the two modes making up one of these  $E$  irreps are degenerate. However, this degeneracy is broken by the FM order, which induces a non-zero Berry curvature via the SOC as discussed Sec. II.

We first present our results for the case of the  $E_g$  and  $E_u$  phonons in Table I. The energy shifts  $\Delta E$  represent the differences between the bare phonon frequencies  $E_0$  computed using only the force-constant term  $K^{(pp)}$

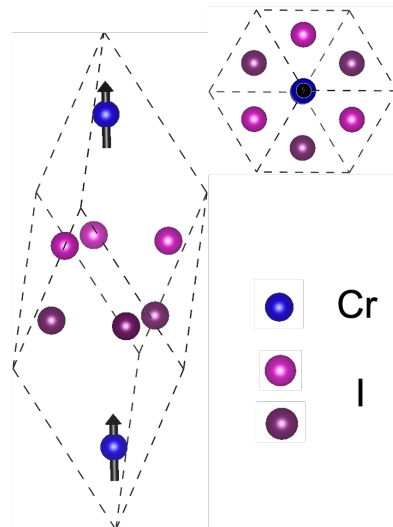


FIG. 1. Visualization of crystal structure and magnetic moments of bulk CrI<sub>3</sub> unit cell. Cr atoms are depicted in blue, while top-layer and bottom-layer I atoms are in bright and dark magenta, respectively. The black vectors indicate the magnetic moments, which are oriented along the  $z$ -direction.

TABLE I. Computed properties of zone-center  $E_g$  and  $E_u$  phonons in bulk CrI<sub>3</sub>. Energy shifts  $\Delta E$  are defined relative to the bare phonon energies  $E_0$ , and are shown for both the full method and the spin-phonon model.  $\chi(C_3)$  is the  $C_3$  eigenvalue indicating the chirality of the mode ( $\varepsilon = e^{2\pi i/3}$ ), and  $L_z$  is the phonon angular momentum of Eq. (15).

Irrep	bare		present approach		spin-phonon	
	$E_0$ (meV)	$\Delta E$ (meV)	$L_z$ ( $\hbar$ )	$\Delta E$ (meV)	$\chi(C_3)$	
$E_g$	7.0000	-0.0017	0.1259	-0.0013	$\varepsilon^*$	
		0.0022	-0.1264	0.0016	$\varepsilon$	
	12.9288	-0.0007	-0.1325	-0.0005	$\varepsilon^*$	
		0.0007	0.1351	0.0006	$\varepsilon$	
	13.4876	-0.0007	0.1740	-0.0002	$\varepsilon^*$	
		0.0007	-0.1761	0.0003	$\varepsilon$	
29.8518	-0.0028	0.8325	$-1.26 \times 10^{-6}$	$\varepsilon^*$		
	0.0028	-0.8326	$1.31 \times 10^{-6}$	$\varepsilon$		
$E_u$	10.7687	-0.0052	0.2352	-0.0045	$\varepsilon$	
		-0.0009	-0.2344	-0.0016	$\varepsilon^*$	
	14.3295	-0.0170	0.7173	-0.0175	$\varepsilon$	
		-0.0042	-0.7192	-0.0040	$\varepsilon^*$	
	27.8225	0.0037	0.9537	-0.0035	$\varepsilon^*$	
	0.0272	-0.9545	0.0356	$\varepsilon$		

in Eq. (9), and the modified energy obtained from the present approach of Eq. (10) or from the spin-phonon model of Appendix B.<sup>3</sup> The PAM  $L_z$  of each phonon is also reported for the present approach.

<sup>3</sup> The results presented in Table I for the spin-phonon model differ from those in Ref. [33] because in this paper, all matrices are calculated using DFT, while in Ref. [33], experimental magnon energies are used to evaluate  $K^{(ss)}$ , and the approximation in Eq. (B6) is taken.



From Table I we observe that all  $E_g$  and  $E_u$  bare phonons are doubly degenerate, while the degeneracy is broken for the perturbed phonons. Although our numerical solution for the bare modes initially yields a pair of real phonons  $|u_1\rangle$  and  $|u_2\rangle$ , we resolve these into eigenstates of the  $C_3$  symmetry operator. We first ensure that  $\langle u_2|C_3|u_1\rangle$  is positive, flipping the sign of  $|u_2\rangle$  if not, and then construct the bare chiral modes  $|u_{\pm}\rangle = (|u_1\rangle \mp i|u_2\rangle)/\sqrt{2}$  belonging to eigenvalues  $\varepsilon = \exp(i2\pi/3)$  and  $\varepsilon^* = \exp(-i2\pi/3)$  respectively. We shall designate these as ‘+’ and ‘-’ modes, and refer to them as belonging to the  $\varepsilon$  and  $\varepsilon^*$  symmetry sectors, respectively. The former (latter) are characterized by a clockwise (counterclockwise) rotation of the Cr atoms when viewed from above.

The numerical solutions for the perturbed phonons automatically generate chiral  $C_3$  eigenstates, and we find that each of these is almost identical to the bare chiral mode of the same symmetry that is closest in energy. There is only a small admixture of other bare modes belonging to the same sector. This allows a straightforward association of bare and perturbed modes as shown in Table I.

Table I demonstrates that the  $E_u$  phonons with  $\varepsilon$  chirality have the largest energy corrections. This follows from their close energy proximity to the  $E_u$  magnons, which also possess  $\varepsilon$  chirality. A detailed discussion of magnons in bulk  $\text{CrI}_3$  is provided in Sec. IV A 2, and a perturbative treatment of phonon-magnon interactions is presented in Appendix D. The pronounced effect on the  $E_u$  phonons is further evident in Eq. (D20), where the phonons with  $\varepsilon$  chirality have the smallest energy denominators.

We briefly address the expected uncertainties in our first-principles calculations of the  $K^{(\text{sp})}$ ,  $G^{(\text{sp})}$ , and  $G^{(\text{pp})}$  matrices, as these are the matrices that contribute to the energy shifts (see Appendix D). First, we analyze the fitting errors for  $K^{(\text{sp})}$  associated with our finite-difference methodology, which is done via linear regression of the forces against spin canting angles. We find that the norm of the fitting error is roughly 1.5% of the norm of  $K^{(\text{sp})}$  itself. A second useful metric is the norm of the residual resulting from symmetrization of a matrix relative to the norm of the matrix itself, which we find to be 0.4%, 2.0%, and 2.7% for  $K^{(\text{sp})}$ ,  $G^{(\text{sp})}$ , and  $G^{(\text{pp})}$  respectively. The perturbation analysis of Eqs. (D20) and (D32) indicates that the energy shifts and splittings are quadratic in  $K^{(\text{sp})}$  and  $G^{(\text{sp})}$  and linear in  $G^{(\text{pp})}$ . This implies overall errors on the order of 3-4% in the values reported above for these shifts and splittings.

In Fig. 2, we visualize the real and imaginary parts of two  $E_g$  chiral phonons around 7 meV, denoted as  $E_g^{(1)}$  for the mode with lower energy and  $E_g^{(2)}$  for the mode with higher energy. It is apparent that those two chiral phonons are approximately complex conjugates of each other.

Note that the argument about energy splitting based on point group irreps can be generalized to any magnetic

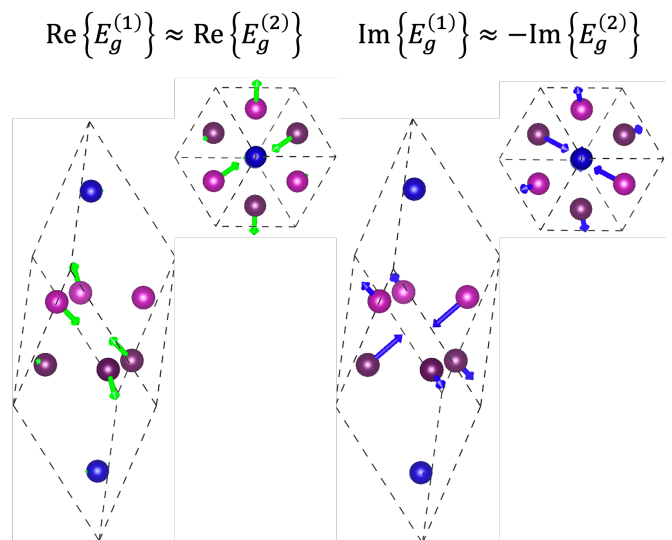


FIG. 2. Visualization of the real and imaginary components of the chiral phonons  $E_g^{(1)}$  and  $E_g^{(2)}$ . Cr atoms are depicted in blue, while top-layer and bottom-layer I atoms are in bright and dark magenta, respectively. The green vectors represent the real part of the phonon displacement, and the blue vectors represent the imaginary part. The real part of  $E_g^{(1)}$  and  $E_g^{(2)}$  are nearly identical, while the imaginary parts are in opposite directions.

material with a point group that includes an  $E$ -type irrep ( $E$ ,  $E_g$ , or  $E_u$ ) consisting of two 1D irreps when complex representations are allowed, indicating that similar phonon energy splittings can be expected in such materials.

The phonon angular momentum is calculated using Eqs. (14) and (15), and the results are listed in Table I. Due to the  $C_3$  symmetry, the total angular momentum of a given chiral phonon can only have a  $z$ -component. We find values of  $|L_z|$  ranging from 0.13 to 0.95 in units of  $\hbar$ , indicative of a substantial angular momentum for many of the chiral phonons, especially the higher-frequency ones.

We find that the bare circular modes, constructed as  $|u_{\pm}\rangle = (|u_1\rangle \mp i|u_2\rangle)/\sqrt{2}$  from the real bare modes, can be used to evaluate the PAM to a good approximation. The results are close to those shown in Table I, with a typical error of  $10^{-3}\hbar$  in  $|L_z|$ . However, when calculating the PAM in this way, the angular momentum vanishes exactly when summed over any pair of chiral phonons, which have equal and opposite  $L_z$  values. In contrast, solutions using the full matrices of Eq. (10) reveal that the cancellation is no longer perfect, and the total angular momentum of a pair is small but non-zero. The slight discrepancy between the two  $|L_z|$  values arises from the magnon-mediated phonon-phonon mixing, which appears at second-order in the phonon-magnon coupling and therefore makes only a minor contribution. We provide a more detailed discussion on this topic based on a perturbation approach in Appendix D 1.

TABLE II. Computed properties of zone-center  $A_g$  and  $A_u$  phonons in bulk  $\text{CrI}_3$ . Energy shifts  $\Delta E$  are defined relative to the bare phonon energies  $E_0$ .  $L_z$  is the phonon angular momentum of Eq. (15).

Irrep	$E_0$ (meV)	$\Delta E$ ( $10^{-8}$ meV)	$L_z$ ( $10^{-4}\hbar$ )
$A_g$	9.95	-8.8	1.99
	11.35	2.6	-2.37
	16.50	-50.6	-1.07
	26.51	98.6	1.96
$A_u$	8.13	-4.5	-1.16
	16.60	-7.9	2.65
	31.74	32.7	-0.52

### 1. Importance of $G^{(\text{pp})}$ and $G^{(\text{ps})}$ in calculating energies

The methodology of Ref. [33] for  $\text{CrI}_3$  differs from the approach of this work (i.e., Eq. (10) and Eq. (11)) in the following ways. First, the only Berry curvature considered in Eq. (11) was  $G^{(\text{ss})}$ . Second, the minimal model in Ref. [33] neglects the mixing between bare phonon doublets, considering the interaction which each doublet and one magnon branch separately. In Appendix B, we discuss a more comprehensive version of that model which still neglects  $G^{(\text{pp})}$ ,  $G^{(\text{sp})}$ , and  $G^{(\text{ps})}$ , but incorporates all bare phonons and magnons. To show the importance of  $G^{(\text{pp})}$  and  $G^{(\text{sp})}$  ( $G^{(\text{ps})}$ ) in accurately determining energy splittings, we also apply the model present in Appendix B to calculate chiral phonon energies for  $E_g$  and  $E_u$  modes, and the results are present in Table I.

As shown in Table I, both methods exhibit an energy splitting of chiral modes compared to bare phonons. The energy splitting of low-energy  $E_g$  and  $E_u$  phonons is similar to that obtained using the present approach, suggesting that  $G^{(\text{pp})}$  and  $G^{(\text{ps})}$  have little effect on those modes. However, for high-energy  $E_g$  and  $E_u$  phonons, the spin-phonon model results differ significantly, indicating the importance of  $G^{(\text{pp})}$  and  $G^{(\text{ps})}$  for these phonons. Specifically, the absolute values of the  $G^{(\text{pp})}$  matrix elements for these four  $E_g$  modes are  $\{0.995, 0.254, 0.972, 5.623\}$  in units of  $\mu\text{eV}$ . The highest-energy  $E_g$  modes exhibit substantially greater values, leading to a pronounced energy splitting. Appendix D 3 details the perturbative analysis of  $G^{(\text{pp})}$ , with Eq. (D32) specifying the energy corrections attributed to the  $G^{(\text{pp})}$  term. As indicated by Eq. (D32),  $G^{(\text{pp})}$  primarily accounts for the substantial splitting observed in the highest-energy  $E_g$  mode, with both direct computation and perturbative treatment yielding a correction of  $\pm 0.0028$  meV.

Interestingly, we find that the PAM calculated using the spin-phonon model (not shown) is in good agreement with the full method with an error of the order of  $10^{-4}\hbar$ , suggesting that the phonon vectors are not very different regardless of whether  $G^{(\text{pp})}$  and  $G^{(\text{ps})}$  are included or not.

We now turn to a consideration of the  $A_g$  and  $A_u$  modes. The spin-phonon model presented in Appendix B has no effect on the  $A_g$  and  $A_u$  phonons, since  $K^{(\text{sp})}$

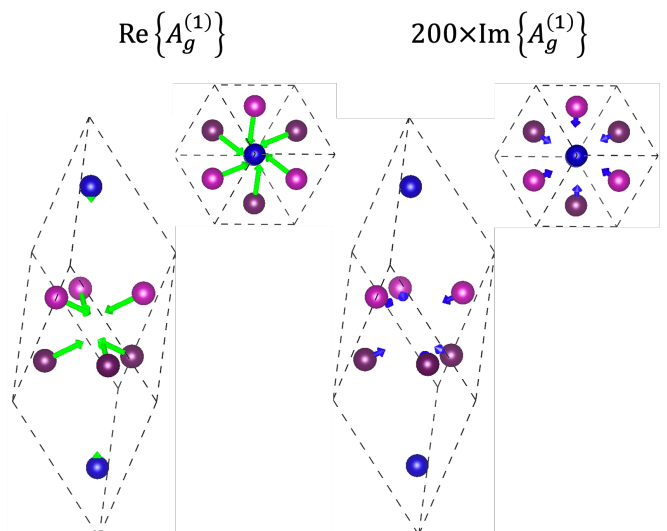


FIG. 3. Visualization of the real and imaginary components of the perturbed phonon  $A_g^{(1)}$ . Cr atoms are depicted in blue, while top-layer and bottom-layer I atoms are in bright and dark magenta, respectively. The green vectors represent the real part of the phonon displacement, and the blue vectors represent the imaginary part, which are amplified 200 times.

gives the coupling to magnons, and there are no zone-center magnons in these symmetry sectors. Considering the present approach, although all (ss) and (sp) terms are absent in the  $A_g$  and  $A_u$  sectors, the  $G^{(\text{pp})}$  matrix does not vanish, and causes a slight mixing between two different  $A_g$  (or  $A_u$ ) bare phonons. That is, we can write  $|u_n\rangle \simeq |u_n^{(0)}\rangle + i \sum_m \delta_m |u_m^{(0)}\rangle$ , where  $|u_{\{n,m\}}^{(0)}\rangle$  represents the bare phonons from  $A_g$  (or  $A_u$ ) irrep. Here,  $i\delta_m$  is purely imaginary and expected to be small, attributed to the minor size of  $G^{(\text{pp})}$  matrix element, as discussed in Appendix D 3.

This results in a nonzero PAM and nonzero energy shift of each phonon relative to its bare energy. Although these phonons exhibit non-zero PAM, we refrain from referring to them as “chiral phonons” because they belong to the  $\chi(C_3) = 1$  sector of modes that are invariant under the  $C_3$  operation. Instead, we refer to them as  $(1 + i\delta)$ -type perturbed phonons, or simply perturbed phonons.

The energy shifts and PAM for  $A_g$  and  $A_u$  perturbed phonons are presented in Table II, and the real and imaginary parts of the  $A_g$  perturbed phonon near 10 meV ( $A_g^{(1)}$ ) are visualized in Fig. 3.

### 2. Bare and perturbed magnons

So far we focused solely on the phonon-like solutions of the equation of motion given by Eq. (10) in the present approach (or Eq. (B1) for the spin-phonon model). Nevertheless, these equations also admit magnon-like solutions, which we call “perturbed magnons.” In this sec-

TABLE III. Energies of the bare magnons  $E_0$ , energy shifts of perturbed magnon modes comparing to bare magnons  $\Delta E$ , and the corresponding  $C_3$  eigenvalues  $\chi(C_3)$  for both  $E_g$  and  $E_u$  modes in bulk  $\text{CrI}_3$ .

Irrep	$E_0$ (meV)	$\Delta E$ (meV)	$\chi(C_3)$
$E_g$	0.5902	-0.0046	$\varepsilon$
$E_u$	22.8635	-0.0224	$\varepsilon$

tion, we investigate the impact of phonons on the magnon spectrum, using bulk  $\text{CrI}_3$  as a case study. The numerical values for the matrices  $K^{(ss)}$  and  $G^{(ss)}$  are provided in Appendix C.

The EOM for a bare magnon without any phonon-magnon interaction is given by Eq. (12). The energies of bare magnons are listed in Table III. The  $E_g$  magnon corresponds to the acoustic mode, where the two Cr spins have the same canting, while the  $E_u$  magnon corresponds to the optical mode, where the two Cr spins have opposite canting. Both magnons have positive energies and belong to the ‘+’ sector with  $\chi(C_3) = \varepsilon$ , indicating that the two Cr spins are rotating clockwise.<sup>4</sup>

The perturbed magnons have slightly modified energies (Table III). The energy change from the bare magnon for the  $E_u$  mode is more significant compared to the  $E_g$  magnon, since the  $E_u$  phonons are closer to the  $E_u$  magnon in the energy spectrum. By far the most significant contribution to the energy shifts is the inclusion of  $K^{(sp)}$ ; neglecting the  $G^{(pp)}$ ,  $G^{(sp)}$ , and  $G^{(ps)}$  terms changes the energies by less than  $0.4 \mu\text{eV}$ . A perturbation treatment of magnon energies is provided in Appendix D 1.

Note that the equations of motion have two additional negative-energy magnon solutions belonging to the ‘-’ sector with  $\chi(C_3) = \varepsilon^*$ . These correspond to the counterclockwise precession of spins and are not physically observable. Nonetheless, they still influence the system dynamics through their interaction with physical ‘-’ phonons, which acquire some magnon dressing in which the spin vectors are forced to precess in the unnatural counterclockwise sense. This becomes clear from the perturbation analysis presented in Appendix D, where the summation index  $\mu$  in Eq. (D16) and Eqs. (D19-D20) runs over all solutions of Eq. (D3), including those of negative energy. However, since the energy denominators in Eq. (D20) are larger when coupling to negative-energy solutions, the magnon dressing is typically smaller. This explains why the ‘+’ phonons, which couple to positive-energy magnon solutions, are more strongly perturbed than the ‘-’ ones, which do not. This can be seen in Table I, where it is especially noticeable for the  $E_u$  modes.

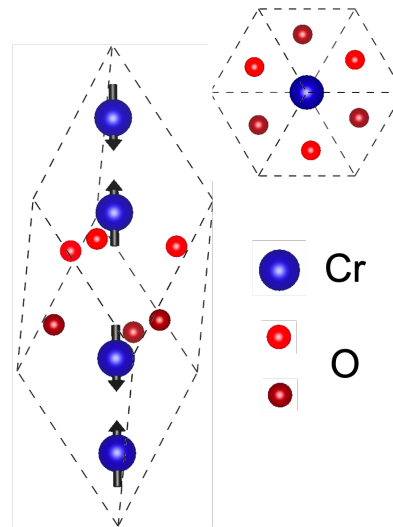


FIG. 4. A visualization of the crystal structure and magnetic moments of the unit cell of bulk  $\text{Cr}_2\text{O}_3$ . The Cr atoms are depicted in blue, while the top-layer and bottom-layer O atoms are shown in bright and dark red, respectively. The black vectors indicate the magnetic moments, which are oriented along the  $z$ -direction.

## B. Phonons in antiferromagnetic $\text{Cr}_2\text{O}_3$

In this section, we present our results for the phonons in bulk  $\text{Cr}_2\text{O}_3$ . As shown in Fig. 4,  $\text{Cr}_2\text{O}_3$  has an AFM insulating ground state with antiparallel magnetic moments aligned along the threefold-rotational  $z$  axis.

The magnetic symmetry of  $\text{Cr}_2\text{O}_3$  is richer than that of  $\text{CrI}_3$ , in that it belongs to a Type III (“black-white”) magnetic group [69]. Since we are interested in zone-center phonons, we frame our discussion in terms of the magnetic point group  $\mathcal{G}$ . The black-white character means that half the the elements of  $\mathcal{G}$  come with the TR operator  $\mathcal{T}$  and half come without. The latter form a “unitary subgroup”  $\mathcal{H}$ , and the others are of the form  $g\mathcal{H}$  where  $g$  is one of the antiunitary operators in  $\mathcal{G}$ . The “structural point group”  $\bar{\mathcal{G}}$  contains the same list of operators as in  $\mathcal{G}$ , except that  $\mathcal{T}$  is removed from all the antiunitary operators. The important point in what follows is that while the Hessian matrices are even under all elements of  $\bar{\mathcal{G}}$ , the Berry curvature matrices are even under the elements of  $\mathcal{H}$  and odd under the elements of  $\bar{\mathcal{G}} - \mathcal{H}$ . As a consequence, when the Berry curvature is included, the irreps of unitary subgroup  $\mathcal{H}$ , not the structural group  $\bar{\mathcal{G}}$ , should be used to label the perturbed modes of this system.

In the case of  $\text{Cr}_2\text{O}_3$ , the magnetic space group is  $R\bar{3}'c'$ , and the structural point group is  $D_{3d}$ . The magnetic ordering on the Cr sublattice breaks inversion ( $i$ ), dihedral mirror ( $\sigma_d$ ), and rotoinversion ( $S_6$ ) symmetries, reducing the unitary point group to  $D_3$ , whose irreps will be used to label our perturbed phonons and magnons. The corresponding time-reversed operators  $i\mathcal{T}$ ,  $\sigma_d\mathcal{T}$ , and  $S_6\mathcal{T}$  are present in the magnetic point group, but being antiuni-

<sup>4</sup> It is important to clarify that the reference to the clockwise rotation of the two spins is in the context of their motion as viewed from the direction of  $s_z$ . However, viewed from the direction of  $M_z$ , which is opposite to  $s_z$ , the two magnetic moments still rotate counterclockwise in the  $(M_x, M_y)$  plane.

TABLE IV. Bare phonon irreps, energies, atom-resolved phonon angular momentum (ARPAM) of Cr atoms in  $z$ -direction (Cr  $L_z$ ), ARPAM of O atoms in  $x$ -direction (O  $L_x$ ), and inter-irrep mixing ( $\rho$ ) of perturbed phonons in bulk Cr<sub>2</sub>O<sub>3</sub>. The bare phonon energies  $E_0$  are included as a reference for the energy shifts  $\Delta E$ .  $E$ -irrep ( $E_g$  and  $E_u$ ) phonons are doubly degenerate. Note that ‘0’ denotes an entry that is precisely zero by symmetry, while ‘0.000’ signifies a non-zero entry that has been rounded to zero. The energy shifts  $\Delta E$  for  $A$ -irrep perturbed phonons are on the order of  $10^{-4}$   $\mu\text{eV}$ , and  $L_x$  for the O atom of the  $A_{2g}^{(1)}$  phonon at 33.310 meV is  $9 \times 10^{-9}\hbar$ .

Irrep	$E_0$ (meV)	$\Delta E$ ( $\mu\text{eV}$ )	Cr $L_z$ ( $10^{-4}\hbar$ )	O $L_x$ ( $10^{-4}\hbar$ )	$\rho$ ( $10^{-4}$ )
$E_g$	36.458	-0.399	-2.087	-0.227	4.319
	43.739	-1.738	1.302	0.171	2.219
	49.602	-0.438	-0.073	0.175	1.104
	65.043	-0.124	-0.125	-0.037	2.592
	76.667	0.355	0.583	-1.471	10.547
$E_u$	38.209	-0.010	0.485	0.213	4.877
	55.803	-0.095	0.231	0.314	1.086
	67.431	1.161	1.537	-0.012	5.785
	76.041	0.023	-0.064	0.371	10.231
$A_{1g}$	36.326	0.000	0	0	0.225
	67.779	0.000	0	0	0.219
$A_{1u}$	51.723	0.000	0	0	0.335
	77.221	0.000	0	0	0.203
$A_{2g}$	33.310	0.000	0	0.000	0.727
	56.989	0.000	0	0.517	2.270
	83.594	0.000	0	-0.161	1.319
$A_{2u}$	50.565	0.000	0	0.090	1.784
	67.760	0.000	0	-0.604	2.212

tary, do not induce any additional irreps.

While the experimental magnetic moment of Cr<sub>2</sub>O<sub>3</sub> is found to be along the  $z$  direction, DFT calculations predict an in-plane magnetic moment. This discrepancy can be resolved by applying a 2% epitaxial strain, which results in an easy-axis ground state [62]. To ensure consistency with the experimental ground state, we apply a 2% epitaxial strain in our calculations, as our model assumes spins to be oriented along the  $z$ -direction.

As previously discussed, the irreps of point group  $D_3$  should be used to characterize zone-center perturbed phonons, which can be decomposed into  $4A_1 \oplus 6A_2 \oplus 10E$ . Among them, one  $A_2$  and two  $E$  modes correspond to acoustic phonons. According to the character table of  $D_3$ , the  $E$  irreps have to be 2D irreps, indicating that there is no degeneracy breaking or energy splitting compared to bare phonons. This is confirmed by the numerical results of perturbed phonon energies, which are presented in Table IV. It is worth noting that the perturbed phonon energies differ from those of the bare phonons, which are also included in Table IV for reference purposes.

### 1. Mixing of phonon irreps

As mentioned earlier, although  $i$ ,  $\sigma_d$ , and  $S_6$  are no longer symmetries,  $i\mathcal{T}$ ,  $\sigma_d\mathcal{T}$ , and  $S_6\mathcal{T}$  remain symmetries of the system. On the other hand, the matrices  $K^{(\text{pp})}$  and  $M^{(\text{pp})}$  are both real. Applying the symmetry operations  $i\mathcal{T}$ ,  $\sigma_d\mathcal{T}$ , and  $S_6\mathcal{T}$  to these matrices is equivalent to applying  $i$ ,  $\sigma_d$ , and  $S_6$ , respectively. Therefore,  $K^{(\text{pp})}$  and  $M^{(\text{pp})}$  are symmetric not only under the  $D_3$  symmetry operations, but also under  $i$ ,  $\sigma_d$ , and  $S_6$ , resulting in a point group symmetry of  $D_{3d}$ .

This has an important impact on the symmetries of zone-center bare phonons, which are calculated using  $K^{(\text{pp})}$  and  $M^{(\text{pp})}$ : bare phonons at the  $\Gamma$  point must have  $D_{3d}$  symmetry, and thus can be labeled by the irreps of  $D_{3d}$ . The  $\Gamma$  point bare phonons decompose into  $5E_g \oplus 5E_u \oplus 2A_{1g} \oplus 2A_{1u} \oplus 3A_{2g} \oplus 3A_{2u}$ , where one  $E_u$  doublet and one  $A_{2u}$  mode are acoustic modes. The irreps of the bare phonons are included in Table IV.

The presence of magnetic moments in bulk Cr<sub>2</sub>O<sub>3</sub> results in the breaking of  $i$ ,  $\sigma_d$ , and  $S_6$  symmetries associated with the bare phonons. Consequently, the original  $D_{3d}$  point group symmetry is reduced to  $D_3$ , leading to inter-irrep mixing between bare phonons of different irreps. Referring to the correlation table of the  $D_{3d}$  point group, we find that the  $E_g$  and  $E_u$  irreps combine to form the  $E$  irrep, the  $A_{1g}$  and  $A_{1u}$  combine to form the  $A_1$  irrep, and the  $A_{2g}$  and  $A_{2u}$  irreps combine to form the  $A_2$  irrep of  $D_3$ . An important question arises: How significant is this inter-irrep mixing, and to what extent does the spatial symmetry breaking due to the magnetic order impact the behavior of the phonons?

To address this question, we project the bare phonons belonging to irreps of the  $D_{3d}$  group onto the perturbed phonons. This allows us to determine the components of each irrep in  $D_{3d}$  that contribute to the given perturbed phonon. We introduce the concept of irrep decomposition component, denoted as  $\rho_n(\text{irrep})$ , which is defined as

$$\rho_n(\text{irrep}) = \left( \sum_{m \in \text{irrep}} | \langle u_m^{(0)} | M^{(\text{pp})} | u_n \rangle |^2 \right)^{\frac{1}{2}}, \quad (29)$$

where  $n$  is the label for the perturbed phonon mode and  $m$  runs over bare phonons from a particular irrep. The last column of Table IV reports our results for  $\rho_n(E_u)$  for  $n \in E_g$  and vice versa, and similarly for  $A_{1g}$ - $A_{1u}$  and  $A_{2g}$ - $A_{2u}$  components. In each case, the majority component (e.g.,  $\rho_n(E_g)$  for  $n \in E_g$ ) is almost unity, so we list only the minority components. These are non-zero as expected, but we find them to be quite small, typically between  $10^{-3}$  and  $10^{-4}$ . This implies that the phonon sector exhibits only weak breaking of inversion symmetry, allowing us to continue to refer to the perturbed phonons as  $E_g$ -like or  $E_u$ -like.



TABLE V. Raman and infrared (IR) activities for bare and perturbed phonons. For perturbed phonons, the Irrep\* column indicates the irrep of perturbed phonons labeled by irreps of  $D_{3d}$ , which is made possible by the weak inter-irrep mixing. In cases where a perturbed phonon exhibits both Raman and IR activity, the minor activity is presented within parentheses and is subordinate to the major activity.

Bare phonons		Perturbed phonons		
Irrep	Activity	Irrep	Irrep*	Activity
$E_g$	Raman	$E$	$E_g$ -like	Raman (IR)
$E_u$	IR	$E$	$E_u$ -like	IR (Raman)
$A_{1g}$	Raman	$A_1$	$A_{1g}$ -like	Raman
$A_{1u}$		$A_1$	$A_{1u}$ -like	Raman
$A_{2g}$		$A_2$	$A_{2g}$ -like	IR
$A_{2u}$	IR	$A_2$	$A_{2u}$ -like	IR

## 2. Experimental implications: Raman and infrared activity

The experimental implication of the inter-irrep mixing is that the perturbed phonons will exhibit distinct Raman and IR activities compared to bare phonons, as summarized in Table V. Above the Néel temperature, where TRS is preserved, the symmetry of the phonons corresponds to that of the bare phonons, so that  $E_u$  phonons are IR-active but Raman-inactive. However, upon cooling the sample below the Néel temperature,  $E_u$  phonons undergo mixing with  $E_g$  phonons, resulting in the emergence of  $E_u$ -like perturbed phonons. These  $E_u$ -like phonons possess Raman activity (in addition to IR activity), as they technically belong to the  $E$  irrep of the  $D_3$  point group. However, since the inter-irrep mixing is small, the Raman activity of the  $E_u$ -like phonons is relatively weak. Nonetheless, recent Raman measurements have confirmed the presence of these features [70]. In a similar way, the Raman-active  $E_g$ -like phonons acquire some small IR activity. Clearly, an approach such as ours, which treats the coupling of phonons and spins in a realistic and symmetry-consistent manner, is needed to describe these effects.

## 3. Atom-resolved phonon angular momentum

As mentioned earlier, inversion is no longer a symmetry in  $\text{Cr}_2\text{O}_3$ , but inversion times time reversal ( $i\mathcal{T}$ ) remains a symmetry. This means that  $i\mathcal{T}$  maps total angular momentum from  $\vec{L}$  to  $-\vec{L}$ , resulting in  $\vec{L} = \vec{0}$  for any non-degenerate single mode or for the sum over two degenerate modes. However, each atom can still possess a nonzero atom-resolved phonon angular momentum (ARPAM), defined by Eqs. (14) and (15) above. ARPAM is a pseudovector assigned to each atom and has the same symmetry as a local magnetic moment. The configuration of the local magnetic moment is determined by the magnetic space group, and this is also true for the ARPAM.

TABLE VI. Possible configurations of atom-resolved phonon angular momentum (ARPAM) for bulk  $\text{Cr}_2\text{O}_3$  according to the magnetic space group  $R\bar{3}'c'$ . Cr atoms can only have out-of-plane angular momentum  $L_z$  or  $-L_z$ , while O atoms can only have in-plane angular momentum and must respect  $C_3$  symmetry.

Atom	Wyckoff positions	ARPAM
Cr	12c	$(0, 0, L_z), (0, 0, -L_z)$
O	18e	$\{I, C_3, C_3^2\} \cdot (L_x, 0, 0)$

For  $\text{Cr}_2\text{O}_3$ , Cr and O atoms occupy Wyckoff positions 12c and 18e respectively. The possible configurations of ARPAM (and local magnetic moments) are listed in Table VI<sup>5</sup>, indicating that Cr atoms can only have out-of-plane angular momentum  $L_z$  or  $-L_z$ , while O atoms can only have in-plane angular momentum in a way that respects  $C_3$  symmetry. This is further supported by the numerical results presented in Table IV. In Fig. 5, we visualize the ARPAM for the  $E_g^{(1)}$  perturbed phonon around 36 meV and the  $A_{2g}^{(2)}$  perturbed phonon near 57 meV, where the  $L_z$  for Cr atoms and the in-plane angular momentum for O atoms are clearly visible.

It is important to note that there exists a gauge freedom for each  $E$  doublet, where the two degenerate modes can be unitarily mixed with each other through a  $U(2)$  matrix. Therefore, discussing ARPAM for each individual  $E$  mode is meaningless, as it is gauge-dependent. However, the sum of ARPAM for the two degenerate  $E$  modes is gauge-independent. To demonstrate this, let us consider an  $E$  doublet labeled by  $n = \{1, 2\}$ , where  $L_{n,Iz}$  denotes the ARPAM for atom  $I$  along the  $z$ -direction. Then, the sum of  $L_{1,Iz}$  and  $L_{2,Iz}$  is

$$\begin{aligned}
 & L_{1,Iz} + L_{2,Iz} \\
 &= \hbar M_I \text{Tr} \left[ \begin{pmatrix} u_{1,Ix}^* & u_{1,Iy}^* \\ u_{2,Ix}^* & u_{2,Iy}^* \end{pmatrix} \begin{pmatrix} 0 & -i \\ i & 0 \end{pmatrix} \begin{pmatrix} u_{1,Ix} & u_{2,Ix} \\ u_{1,Iy} & u_{2,Iy} \end{pmatrix} \right] \\
 &= 2\hbar M_I [\text{Im}(u_{1,Ix}^* u_{1,Iy}) + \text{Im}(u_{2,Ix}^* u_{2,Iy})], \quad (30)
 \end{aligned}$$

which is the trace of a product of three matrices. While different gauges correspond to different bases for these matrices, they do not affect the trace, making  $L_{1,Iz} + L_{2,Iz}$  a gauge-invariant quantity. This is also true for the  $x$  and  $y$  directions. The ARPAM for  $E$ -irrep perturbed phonons shown in Table IV is traced over the two degenerate modes in the doublet. For  $E$  modes with nonzero ARPAM, there is no gauge choice in the degenerate subspace where the phonon mode displacements can be expressed as purely real eigenvectors.

<sup>5</sup> Based on the Bilbao crystallography server [71–73] (through the MWYCKPOS module [74]).

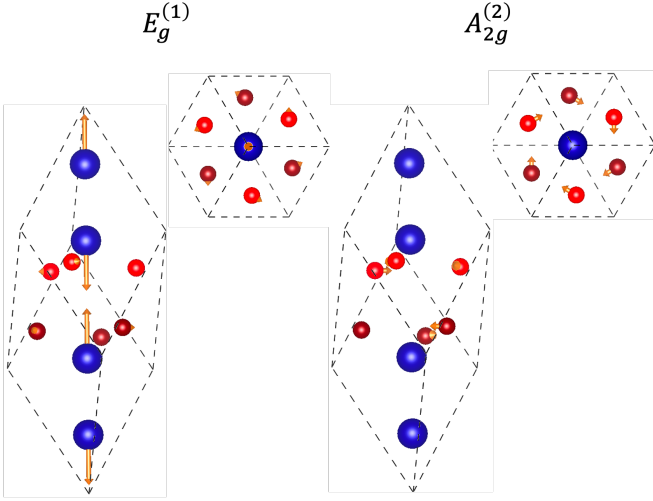


FIG. 5. Atom-resolved phonon angular momentum (ARPAM) for two selected modes in bulk  $\text{Cr}_2\text{O}_3$ :  $E_g^{(1)}$ -like mode near 36 meV and  $A_{2g}^{(2)}$ -like mode near 57 meV. The ARPAM for the  $E_g$ -like mode is traced over two degenerate modes. The amplitude of ARPAM in this figure is amplified by a factor of 1000 compared to Fig. 6.

#### 4. Chiral decomposition of $E$ modes

Despite the fact that perturbed  $E$  phonons are always doubly degenerate, it is still worthwhile to decompose the doublet into two single  $E$  chiral phonons that respect  $C_3$  symmetry individually and have complex eigenvalues. There are several reasons for this. Firstly, these chiral phonons are excited by circular polarized photons [45]. Secondly, they exhibit different energies in the presence of an external magnetic field along the  $z$ -direction. Finally, these modes correspond to a special gauge choice in which each individual mode has the largest  $L_z$  magnitude. To decompose the  $E$  doublets, we diagonalize the  $C_3$  matrix using the bases formed by two degenerate  $E$  modes. The resulting eigenvectors correspond to two  $E$  chiral phonons that respect  $C_3$  symmetry individually. Since the two  $E$  modes together respect the  $C_3$  symmetry, the  $C_3$  matrix has to be a  $2 \times 2$  unitary matrix, and is therefore diagonalizable.

We have decomposed the  $E_g$ -like perturbed phonons around 36 meV into two chiral phonons, denoted as  $E_g^{(1)+}$  and  $E_g^{(1)-}$ , and have visualized their real parts, imaginary parts, and ARPAM in Fig. 6. The real parts of the two modes are almost identical to each other, while the imaginary parts are almost opposite. As a consequence, the ARPAMs of the two modes are also nearly opposite to each other. The PAMs for the ‘+’ and ‘-’ modes are  $\pm 0.8593\hbar$ , respectively. However, the ARPAMs of the two modes do not cancel out perfectly, and their sum is shown in the left panel of Fig. 5. Other  $E_g$ -like and  $E_u$ -like perturbed phonons can also be decomposed in the same manner.

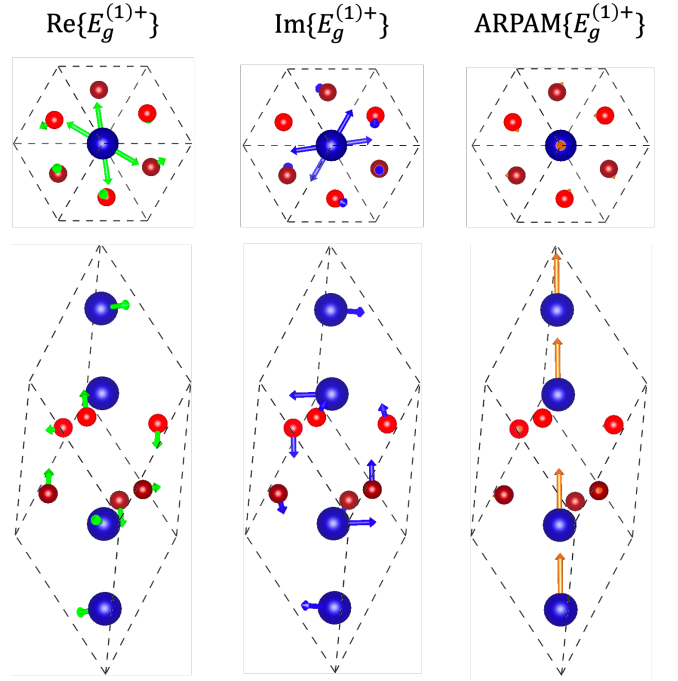


FIG. 6. The real and imaginary components, as well as atom-resolved phonon angular momentum (ARPAM), of the chiral phonon  $E_g^{(1)+}$  around 36 meV in  $\text{Cr}_2\text{O}_3$ . The Cr atoms are shown in blue, while the top-layer and bottom-layer O atoms are depicted in bright and dark red, respectively. The green vectors indicate the real part of the phonon displacement, the blue vectors indicate the imaginary part, and the brown vectors represent the ARPAM. The real parts of  $E_g^{(1)-}$  are almost identical to  $E_g^{(1)+}$ , while its imaginary parts and ARPAM are almost opposite to those of  $E_g^{(1)+}$ .

#### 5. Magnons

We now turn to a discussion of the magnons. As a reminder, bare magnons are solved as described in Sec. IV A 2, while perturbed magnons are magnon-like solutions of the EOM of the present approach. The energies of bare and perturbed magnons are presented in Table VII, and the numerical values for the matrices  $K^{(ss)}$  and  $G^{(ss)}$  describing the bare magnons are given in Appendix C.

We find that bare and perturbed magnons have almost identical energies, which results from the weak SOC for both the Cr and the O atoms. Since magnons belong to the  $E$  irrep, they must be doubly degenerate. These degenerate magnons can be decomposed into two magnons, each with  $\chi(C_3)$  equal to  $\epsilon$  or  $\epsilon^*$ , following the same method we used with  $E$  phonons. Additionally, these magnons can also be excited by circular polarized photons.

We next analyze the symmetries of magnons by considering the  $E_g$  and  $E_u$  components of each magnon mode, in a manner analogous to Eq. (29). Unlike the bare phonons, however, the bare magnons do not have well-

TABLE VII. Energies of the bare magnons ( $E_0$ ) and perturbed magnons ( $E$ ) in bulk  $\text{Cr}_2\text{O}_3$ , as well as their  $E_g$  and  $E_u$  components defined in Eq. (29).

$E_0$ (meV)	$\Delta E$ ( $\mu\text{eV}$ )	$\rho(E_g)$	$\rho(E_u)$
2.423	-0.043	0.0386	0.9993
66.899	-0.045	0.6701	0.7423

defined parity, because the magnetic order strongly violates inversion symmetry. Therefore, we base our analysis on the eigenvectors of the anisotropy matrix  $K^{(ss)}$  instead. Note that  $K^{(ss)}$ , being quadratic in the spin DOF, is real and symmetric, so that the symmetry operator  $i\mathcal{T}$  behaves like  $i$  for  $K^{(ss)}$ . Thus, it has well defined  $E_g$  and  $E_u$  eigenvectors that we denote as  $|t_\mu\rangle$ . Then the  $E_g$  and  $E_u$  components of a general solution  $|s_\mu\rangle$  are defined via

$$\rho_\mu(\text{irrep}) = \left( \sum_{\nu \in \text{irrep}} |\langle t_\nu | s_\mu \rangle|^2 \right)^{1/2}, \quad (31)$$

where both  $|t_\nu\rangle$  and  $|s_\mu\rangle$  are normalized. These  $\rho$  values can be used to quantify the extent to which the inversion symmetry is broken for magnons, and the numerical values are listed in Table VII. We find that the acoustic magnons, which have lower energies, are nearly  $E_u$  modes. However, the optical magnons have comparable  $\rho(E_g)$  and  $\rho(E_u)$  values, indicating that the inversion symmetry is strongly broken for these modes. This is not surprising, and is true also for the bare magnons, since the equations of motion for spin strongly violate TRS.

Note that we apply a 2% epitaxial strain to fix the sign of the magnetic anisotropic energy, which is related to the energy of acoustic magnons. Although the variation of the magnon energies is sensitive to strain, the impact of such variations on the phonon energy corrections is negligible. This is clarified by the perturbative analysis in Appendix D, particularly evident in Eq. (D20). Given that the energy difference between the  $E$  phonons and acoustic magnons is over 30 meV, a 1 meV variation in the magnon energy leads to a change of only about 3% in the phonon energy correction. Thus, changes in acoustic magnon energy, or the magnetic anisotropic energy, do not significantly influence the phonon energy corrections.

### 6. Summary of $\text{Cr}_2\text{O}_3$

In summary, our analysis shows that perturbed phonons possess  $D_3$  symmetry, while bare phonons exhibit  $D_{3d}$  symmetry. The  $E$ -type irreps of both  $D_3$  and  $D_{3d}$  are two-dimensional, implying that there is no energy splitting despite the breaking of TRS. However, an  $E$  doublet can still be decomposed into two chiral phonons with different chiralities that respect  $C_3$  symmetry. These chiral phonons can be excited by circular-polarized photons with different handedness, and their

degeneracy will be lifted if an external magnetic field is present. Each perturbed phonon consists of components from two irreps of bare phonons, yet the level of inter-irrep mixing remains minimal. This characteristic implies that the inversion symmetry within the phonon sector is not strongly broken. Despite this minimal mixing, it is necessary to label perturbed phonons according to the irreps of the unitary subgroup of the magnetic point group. As a result, the infrared and Raman activity properties of these perturbed phonons differ from those of the bare phonons – a phenomenon that is confirmed by recent experimental observations. Magnons belong to the  $E$  irrep, and are therefore doubly degenerate. The magnons are mixtures of  $E_g$  and  $E_u$  sectors, indicating a strong inversion symmetry breaking for magnons.

### C. Perturbed phonons and magnons in 2D systems

In Secs. IV A and IV B, we have investigated chiral phonons in 3D systems, considering both FM and AFM cases. In this section, we shift our focus to 2D systems, specifically a monolayer of FM  $\text{CrI}_3$  and a monolayer of AFM  $\text{VPSe}_3$ .

#### 1. Chiral phonons in the monolayer $\text{CrI}_3$

Bulk  $\text{CrI}_3$  has van der Waals gaps between layers, which allows it to be exfoliated to a 2D single layer while maintaining FM order [68]. In this section, we report our calculations of chiral phonons in monolayer  $\text{CrI}_3$ , with a focus on comparing the results with those in the bulk cases.

The crystal structure of monolayer  $\text{CrI}_3$  is depicted in Fig. 7. The magnetic group  $P\bar{3}1m'$  is a Type-III black-white group, as was the case for bulk  $\text{Cr}_2\text{O}_3$ . The  $\text{CrI}_3$  monolayer has higher structural symmetry than that of bulk  $\text{CrI}_3$  due to the presence of dihedral mirrors ( $\sigma_d$ ) and two-fold rotations about an in-plane axis ( $C'_2$ ) that are absent in the bulk. This results in a structural  $D_{3d}$  point group, which is twice the size of the structural group  $S_6$  of bulk  $\text{CrI}_3$ . However, the newly added symmetries are all antiunitary in the presence of the FM spin ordering, so that the unitary group is again just  $S_6$ .

Thus, we again label the perturbed phonons at  $\Gamma$  using irreps of  $S_6$ , under which they decompose to  $4A_g \oplus 4E_g \oplus 4A_u \oplus 4E_u$ , where one  $A_u$  mode and two  $E_u$  modes are acoustic modes. Similar to bulk  $\text{CrI}_3$ , the  $E_g$  and  $E_u$  irreps in the  $S_6$  point group correspond to two 1D complex irreps rather than a single 2D irrep. As a result, the  $E_g$  and  $E_u$  chiral phonons are no longer doubly degenerate and have energy splittings when compared to bare phonons. We refer to the  $E_g$  and  $E_u$  phonons as chiral phonons because they individually respect  $C_3$  symmetry, but instead of having identity  $C_3$  eigenvalues, they have complex eigenvalues ( $\varepsilon$  or  $\varepsilon^*$ ). In Table VIII, we present the energies, angular momenta, and  $C_3$  eigenvalues of the

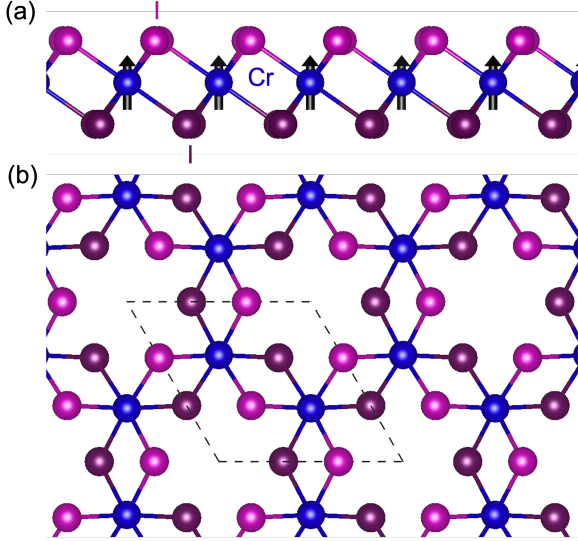


FIG. 7. Side (a) and top (b) views of the crystal structure of monolayer  $\text{CrI}_3$ , with a dashed line indicating the unit cell. Cr atoms are depicted in blue, while top-layer and bottom-layer I atoms are in bright and dark magenta, respectively. The black vectors indicate the magnetic moments, which are oriented along the  $z$ -direction.

$E_g$  and  $E_u$  chiral phonons, along with the energies of the bare phonons as a reference. Additionally, we include the results for magnons.

Comparing Tables VIII and I, we observe that  $E_g$  chiral phonons in monolayer  $\text{CrI}_3$  have a similar energy splitting to those in bulk  $\text{CrI}_3$ , but with larger PAM because the in-plane motion has been enhanced relative to out-of-plane motion. In monolayer  $\text{CrI}_3$ , the  $E_u$  chiral phonons around 10 meV have the largest energy splitting because they are closest in energy to the  $E_u$  magnon. Overall, the mechanisms for  $E_g$  and  $E_u$  chiral phonons in bulk and monolayer  $\text{CrI}_3$  are similar despite differences in energy splittings and magnon energies.

In order to discuss the phonons belonging to the  $A$  irreps, it is essential to first determine the symmetries of the bare phonons. Similar to our argument in bulk  $\text{Cr}_2\text{O}_3$ , since  $\sigma_d\mathcal{T}$  and  $C'_2\mathcal{T}$  remain as symmetries, the bare phonons must possess  $D_{3d}$  symmetries instead of  $S_6$ . We have found that the  $\Gamma$ -point bare phonons can be decomposed into  $2A_{1g} \oplus 2A_{2g} \oplus 4E_g \oplus 1A_{1u} \oplus 3A_{2u} \oplus 4E_u$ , wherein one  $A_{2u}$  mode and two  $E_u$  modes are acoustic. The presence of magnetic moments breaks the  $\sigma_d$  and  $C'_2$  symmetries of the bare phonons, which leads to inter-irrep mixing between the bare phonons of different irreps in the perturbed phonons. According to the correlation table of the  $D_{3d}$  point group, the  $A_{1g}$  and  $A_{2g}$  irreps combine to form the  $A_g$  irrep of  $S_6$ , while the  $A_{1u}$  and  $A_{2u}$  irreps combine to form  $A_u$ . However, as in bulk  $\text{Cr}_2\text{O}_3$ , the inter-irrep mixing in monolayer  $\text{CrI}_3$  is found to be relatively weak, as demonstrated by the results presented in Table IX. This allows us to continue to refer to the perturbed phonons as, e.g.,  $A_{1g}$ -like based on their pre-

TABLE VIII. Energies,  $z$ -direction total PAM ( $L_z$ ), and  $C_3$  eigenvalue ( $\chi(C_3)$ ) of  $E_g$  and  $E_u$  chiral phonons and magnons in monolayer  $\text{CrI}_3$  calculated using the full model. The bare phonon and magnon energies  $E_0$  are included as a reference for the energy shift  $\Delta E$ .

Irrep	$E_0$ (meV)	$\Delta E$ (meV)	$L_z(\hbar)$	$\chi(C_3)$
Phonons				
$E_g$	6.2343	-0.0028	0.1757	$\varepsilon^*$
		0.0033	-0.1762	$\varepsilon$
	12.6725	-0.0005	-0.2398	$\varepsilon^*$
		0.0007	0.2420	$\varepsilon$
	13.4436	-0.0010	0.2234	$\varepsilon^*$
		0.0011	-0.2250	$\varepsilon$
$E_u$	30.1453	-0.0028	0.8408	$\varepsilon^*$
		0.0028	-0.8408	$\varepsilon$
	10.0072	-0.0595	0.2535	$\varepsilon$
		-0.0014	-0.2314	$\varepsilon^*$
	14.2708	-0.0063	-0.7224	$\varepsilon^*$
		0.0450	0.7279	$\varepsilon$
Magnons	28.2112	0.0010	-0.9540	$\varepsilon$
		0.0036	0.9538	$\varepsilon^*$
$E_g$	0.9731	-0.0069		$\varepsilon$
$E_u$	10.5988	-0.0060		$\varepsilon$

dominant character. Nevertheless, it is important to emphasize that the correct labeling of zone-center phonons should consider the irreps of the  $S_6$  group rather than the  $D_{3d}$  group.

Table IX contains the energies, angular momenta, and inter-irrep mixing of  $A_g$  and  $A_u$  perturbed phonons. Bare phonon energies are also included as a reference for the energy shifts. By comparing Tables II and IX, we observe that the perturbed phonons from the  $A$  irreps in both bulk and monolayer  $\text{CrI}_3$  exhibit small energy shifts and have a small PAM, indicating a weak effect of the  $G^{(\text{pp})}$  matrices in both cases.

Concerning the magnons, we find that the energy of the optical magnon in monolayer  $\text{CrI}_3$  is lower than in the bulk. This is attributable to the absence of ferromagnetic inter-layer exchange in the monolayer [75]. In contrast, the energy for the acoustic magnon is greater than that in the bulk. As the acoustic magnon energy is related to the magnetic anisotropy energy (MAE), this suggests a greater MAE for monolayer  $\text{CrI}_3$ . This observation agrees with findings from another study [76], where the generalized-gradient approximation to the exchange-correlation functional was used [77]. The numerical values for the matrices  $K^{(\text{ss})}$  and  $G^{(\text{ss})}$  are provided in Appendix C.

In summary, as is the case for the chiral phonons in bulk  $\text{CrI}_3$ , the  $E_g$  and  $E_u$  chiral phonons in monolayer  $\text{CrI}_3$  are no longer doubly degenerate and possess significant angular momentum. The  $A_g$  and  $A_u$  perturbed phonons exhibit small energy shifts with respect to the bare phonons and acquire non-zero angular momentum. However, unlike the bulk case,  $A_g$  and  $A_u$  perturbed phonons in monolayer  $\text{CrI}_3$  exhibit inter-irrep mixing due



TABLE IX. Energies, total  $z$ -direction PAM ( $L_z$ ), and inter-irrep mixing for  $A$ -irrep perturbed phonons in monolayer  $\text{CrI}_3$ . ‘Irrep’ labels are those of the parent bare phonons, whose energies  $E_0$  are included as a reference for the energy shift  $\Delta E$ .

Irrep	$E_0$ (meV)	$\Delta E$ ( $10^{-8}$ meV)	$L_z$ ( $10^{-4}\hbar$ )	$\rho_n$ ( $10^{-4}$ )
$A_{1g}$	9.47	-6.3	-2.07	1.47
	16.12	-67.4	1.50	2.30
$A_{2g}$	10.92	2.2	2.22	1.72
	26.98	125.4	-2.10	3.77
$A_{1u}$	16.67	-5.0	-2.49	1.37
$A_{2u}$	7.02	-3.7	0.94	0.48
	32.69	27.0	0.49	1.49

to the symmetry reduction caused by the presence of magnetic order. From the perspective of optical activity, the  $A_{2g}$ -like perturbed phonons are weakly Raman-active, since they contain some components from the  $A_{1g}$  sector, whereas the  $A_{1u}$ -like perturbed phonons acquire some IR activity due to components from  $A_{2u}$ .

## 2. Phonons in monolayer $\text{VPSe}_3$

In this section, we investigate the phonons of a  $\text{VPSe}_3$  monolayer, which is a 2D AFM insulator. It is predicted to have a Néel-type AFM structure [63], with the magnetic moment oriented along the  $z$ -direction. The crystal structure of monolayer  $\text{VPSe}_3$  is depicted in Fig. 8. The magnetic space group is  $P\bar{3}'1m$ , which is again a Type-III black-white group. The structural point group is  $D_{3d}$ , but the magnetic moments from V atoms break both inversion ( $i$ ) and two-fold rotational ( $C'_2$ ) symmetries, reducing the unitary point group to  $C_{3v}$ . The three-fold rotation ( $C_3$ ) and dihedral mirror ( $\sigma_d$ ) remain symmetries of the magnetic group, together with operations  $i\mathcal{T}$ ,  $C'_2\mathcal{T}$ , and  $S_6\mathcal{T}$ .

According to the character table for the  $C_{3v}$  point group, the  $E$  irrep is a true 2D irrep, i.e., not a complex conjugate pair of 1D irreps. Therefore, perturbed phonons belonging to  $E$  irreps must be doubly degenerate, which is confirmed by the numerical results in Table X. The energies of the perturbed phonons are described by energy shifts  $\Delta E$  with respect to the bare phonon energies ( $E_0$ ).

The  $\text{VPSe}_3$  monolayer maintains  $i\mathcal{T}$  symmetry, similar to  $\text{Cr}_2\text{O}_3$ . This symmetry forbids the existence of a nonzero total PAM but permits the presence of nonzero ARPAMs. The magnetic space group of  $\text{VPSe}_3$  is  $P\bar{3}'1m$ , with V, P, and Se atoms occupying the  $2c$ ,  $2e$ , and  $6k$  Wyckoff positions, respectively. We find that V atoms possess only nonzero  $L_z$ , Se atoms can only have nonzero in-plane  $\mathbf{L}$ , and P atoms cannot carry angular momentum. The ARPAMs for the perturbed phonons, traced over the subspace of degenerate doublet for phonons with  $E$  irreps, are provided in Table X. It is possible to further decompose the doublets from  $E$  irreps into two chi-

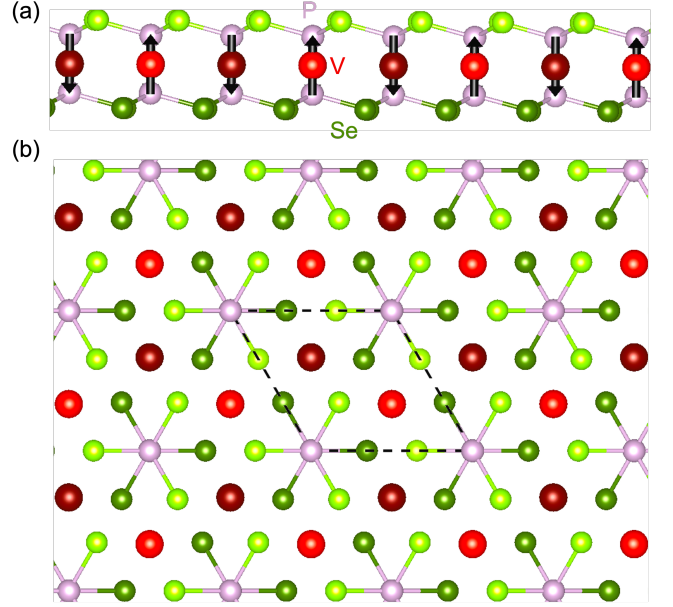


FIG. 8. Side (a) and top (b) views of the crystal structure of monolayer  $\text{VPSe}_3$ , with a dashed line indicating the unit cell. Bright and dark shades denote V atoms with spin up and down, respectively. Purple atoms represent P atoms, while top-layer and bottom-layer Se atoms are in bright and dark green, respectively. The magnetic moments, oriented along the  $z$ -direction, are denoted by black vectors.

ral phonons, which individually respect the  $C_3$  symmetry but have different complex eigenvalues.

Building on our earlier discussion, similar to monolayer  $\text{CrI}_3$  and  $\text{Cr}_2\text{O}_3$ , the  $D_{3d}$  symmetry is preserved by  $K^{(\text{pp})}$  and  $M^{(\text{pp})}$  in monolayer  $\text{VPSe}_3$ , allowing us to use irreps of  $D_{3d}$  to label zone-center bare phonons. These bare phonons decompose to  $5E_g \oplus 5E_u \oplus 3A_{1g} \oplus 4A_{2u} \oplus 1A_{1u} \oplus 2A_{2g}$ , with one  $A_{2u}$  and two  $E_u$  modes being acoustic modes. However, due to the presence of magnetic moments on V atoms,  $i$  and  $C'_2$  symmetries are broken, reducing the symmetry to  $C_{3v}$  and requiring the use of irreps from this point group to label perturbed phonons instead of  $D_{3d}$ . The inter-irrep mixing resulting from the symmetry reduction can be determined from the correlation table, which shows that  $E_g$  and  $E_u$  bare phonons form  $E$  perturbed phonons,  $A_{1g}$  and  $A_{2u}$  bare phonons form  $A_1$  perturbed phonons, and  $A_{2g}$  and  $A_{1u}$  bare phonons form  $A_2$  perturbed phonons. As in the cases of monolayer  $\text{CrI}_3$  and  $\text{Cr}_2\text{O}_3$ , the inter-irrep mixing caused by the magnetic order is small. Thus, we still refer to the perturbed phonons as  $E_g$ -like, etc., but again the correct labeling of those perturbed phonons should involve the irrep of  $C_{3v}$  rather than those of  $D_{3d}$ .

The inter-irrep mixing  $\rho$  is defined in the same manner as with  $\text{Cr}_2\text{O}_3$  using Eq. (29), and the results are presented in Table X. The inter-irrep mixing leads to anomalous Raman/IR activities as well. For example, the  $A_{1g}$ -like and  $E_g$ -like perturbed phonons, which are strongly Raman-active, now acquire small IR activities,

TABLE X. Bare phonon irreps, energies, atom-resolved phonon angular momentum (ARPAM) of V atoms in the  $z$ -direction ( $V L_z$ ), ARPAM of Se atoms in the  $y$ -direction (Se  $L_y$ ), and inter-irrep mixing ( $\rho$ ) of perturbed phonons in monolayer VPSe<sub>3</sub>. Bare phonon energies  $E_0$  are included as a reference for energy shifts  $\Delta E$ . The  $E$ -irrep phonons are doubly degenerate. The energy shifts  $\Delta E$  for  $A$ -irrep perturbed phonons are on the order of  $10^{-5}$   $\mu\text{eV}$ .

Irrep	$E_0$ (meV)	$\Delta E$ ( $\mu\text{eV}$ )	V $L_z$ ( $10^{-4}\hbar$ )	Se $L_y$ ( $10^{-4}\hbar$ )	$\rho$ ( $10^{-4}$ )
$E_g$	12.790	0.052	-0.238	0.008	0.384
	15.102	0.230	0.337	0.707	4.161
	20.127	0.049	-0.055	-0.441	1.116
	27.728	-0.001	-9.280	-0.145	6.013
	53.837	0.016	-0.055	-0.323	26.994
$E_u$	14.526	0.033	-0.453	-0.620	4.269
	18.125	0.049	0.077	0.189	1.029
	30.765	-0.005	11.104	0.171	6.768
	53.697	-0.019	0.039	0.245	26.945
$A_{1g}$	18.743	0.000	0	-0.224	1.154
	25.490	0.000	0	0.050	1.032
	62.327	0.000	0	-0.012	0.357
$A_{2u}$	16.287	0.000	0	0.280	1.101
	32.081	0.000	0	-0.104	0.624
	37.856	0.000	0	-0.142	0.859
$A_{1u}$	16.625	0.000	0	0	0.581
$A_{2g}$	8.955	-0.000	0	0	0.307
	30.688	0.000	0	0	0.220

while IR-active  $A_{2u}$ -like and  $E_u$ -like perturbed phonons acquire small Raman activities. The  $A_{2g}$ -like and  $A_{1u}$ -like perturbed phonons remain silent in both Raman and IR activities.

In addition, we have studied the energies of bare and perturbed magnons. Both bare and perturbed magnons are doubly degenerate as they belong to the  $E$  irrep. The bare magnon energy is found to be 8.58 meV, while the energy shift of the perturbed magnon is  $-0.81$   $\mu\text{eV}$ , which is more significant than in Cr<sub>2</sub>O<sub>3</sub>. This can be attributed to the larger SOC in VPSe<sub>3</sub>. We further analyzed the symmetry of the perturbed magnon by decomposing it into  $E_g$  and  $E_u$  eigenmodes of  $K^{(\text{ss})}$ . Our findings reveal that  $\rho(E_u) = 0.9992$ , while  $\rho(E_g) = 0.0405$ , indicating that the magnon is almost entirely of  $E_u$  symmetry, similar to the acoustic magnon in Cr<sub>2</sub>O<sub>3</sub>. The numerical values for the matrices  $K^{(\text{ss})}$  and  $G^{(\text{ss})}$  are provided in Appendix C.

To summarize, we have computed the perturbed phonons of monolayer VPSe<sub>3</sub>. While bare phonons retain  $D_{3d}$  symmetry, perturbed phonons only possess  $C_{3v}$  symmetry due to the presence of magnetic moments. As in the case of Cr<sub>2</sub>O<sub>3</sub>, the  $E$ -irrep in  $C_{3v}$  is a 2D irrep, preserving degeneracy despite the broken TRS. The total PAM of each perturbed phonon is zero due to  $i\mathcal{T}$  symmetry, but perturbed phonons can possess nonzero ARPAM. Moreover, we have also investigated the energies of bare and perturbed magnons, finding that the energy shift of magnons is greater than in Cr<sub>2</sub>O<sub>3</sub>. Although

the magnon is almost entirely of  $E_u$  symmetry, the  $E_g$ - $E_u$  mixing in the magnon sector is more pronounced than in the phonons.

## V. DISCUSSION

### A. Role of spin-orbit coupling

Spin-orbit coupling (SOC) is essential to the physics described above. We identify three matrices, namely  $K^{(\text{sp})}$ ,  $G^{(\text{sp})}$ , and  $G^{(\text{pp})}$ , all of which either violate TRS or mediate the interaction between phonons and magnons. Here we show that in collinear systems such as those considered here, all three of these matrices vanish in the absence of SOC. Since these matrices control the splittings of degenerate phonon modes, it follows that these splittings also vanish without SOC. This is demonstrated here using formal arguments and then confirmed via numerical calculations on bulk CrI<sub>3</sub>.

In the absence of SOC, the presence of global spin rotational symmetry implies that the exchange interactions are of pure Heisenberg form,  $H = \sum_{\langle ij \rangle} J_{ij} \mathbf{S}_i \cdot \mathbf{S}_j$ , where the  $J_{ij}$  depend on the atomic coordinates. Spin-phonon coupling in noncollinear systems is often described in terms of exchange striction, i.e., the first-order changes of  $J_{ij}$  with atomic displacements (see, e.g., Ref. [78]). However, such variations of  $J_{ij}$  do not induce any spin canting in an SOC-free collinear system. This follows because the energy is stationary with respect to canting of any spin, since  $\delta H = \sum_{\langle ij \rangle} J_{ij} [\mathbf{S}_i \cdot \delta \mathbf{S}_j + \delta \mathbf{S}_i \cdot \mathbf{S}_j]$ , and  $\mathbf{S}_i$  and  $\delta \mathbf{S}_j$  are orthogonal in a collinear spin system.

A complementary point of view comes from noting that the spinor wavefunctions are separable into real spatial wavefunctions with pure spin-up or spin-down character in an SOC-free collinear magnet. This remains true as atoms are displaced, so that there is no induced spin canting. This also explains why  $G^{(\text{pp})}$  vanishes. For example, consider three structural configurations, a reference '0' and configurations with displacements  $\delta q_i$  and  $\delta q_j$ . The Berry phase

$$\Phi_{ij} = -\text{Im} \ln[\langle \psi_0 | \psi_{\delta q_i} \rangle \langle \psi_{\delta q_i} | \psi_{\delta q_j} \rangle \langle \psi_{\delta q_j} | \psi_0 \rangle] \quad (32)$$

clearly vanishes, since all inner products are real.

The argument for the vanishing of  $G^{(\text{sp})}$  is slightly more subtle. This time one of the displacements, say  $\delta q_j$ , is replaced by a spin canting  $\delta s_j$  of one spin. The spin system is no longer collinear, but it is still coplanar. In this case the spinors can be represented using Pauli matrices  $\sigma_3$  and  $\sigma_1$  to span the plane in which the spins lie. Both of these Pauli matrices are real, so the overall spatial-spinor wavefunctions remain real, and the Berry phase around the loop remains zero.

To confirm these conclusions, we repeated the calculation of the spin splittings in bulk CrI<sub>3</sub> while varying the strength of the SOC used in the first-principles calculations. This adjustment required the introduction of a

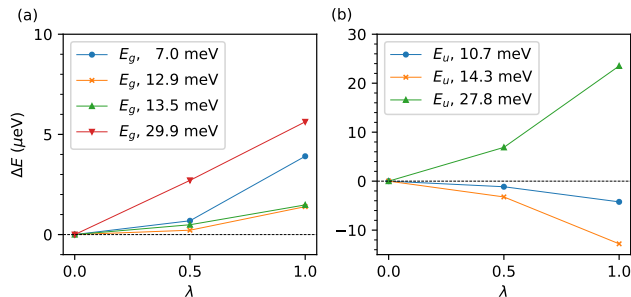


FIG. 9. Energy splittings ( $\Delta E$ ) for the  $E_g$  chiral phonon modes (a) and  $E_u$  chiral phonon modes (b) in bulk  $\text{CrI}_3$ , plotted as a function of the spin-orbit coupling strength scaling factor ( $\lambda$ ). The  $\Delta E$  represents the energy difference between the ‘+’ mode and the ‘-’ mode near that energy.

multiplicative factor in the computational code, followed by recompilation. Figure 9 shows the variation of the phonon energy splittings  $\Delta E$  with the scaling factor  $\lambda$  for the SOC, where  $\lambda = 1$  is the physical strength. Clearly the splittings get smaller as  $\lambda$  is reduced and vanish at  $\lambda = 0$ , consistent with our expectations.

We find that  $K^{(\text{sp})}$ ,  $G^{(\text{sp})}$  and  $G^{(\text{pp})}$  have linear as well as quadratic terms in  $\lambda$  (with the exception of the  $K^{(\text{sp})}$  coupling to acoustic magnons). The quadratic terms are dominant in most cases in Fig. 9, although the linear behavior dominates for the highest-energy  $E_g$  mode.

We emphasize that these conclusions hold for collinear spin systems. While we have not studied noncollinear systems in this work, we fully expect the present approach to apply in that case. In particular, exchange striction will induce bilinear couplings between atomic displacements and spin cantings as captured by our spin-phonon Hessian  $K^{(\text{sp})}$ , even in the absence of SOC. The role of SOC in the spin-phonon coupling of noncollinear systems may be an interesting avenue for future research.

## B. Connection to experiment

Before concluding this paper, we would like to provide some comments on experiments. In materials where chiral phonons exhibit an energy splitting, it is possible to measure this splitting using Raman or IR spectroscopy. Since the splittings for  $E_g$  chiral phonons are usually small, it may be more feasible to measure splittings of  $E_u$  chiral phonons using IR spectroscopy. Additionally, circular-polarized photons with different handedness can excite chiral phonons with different chiralities, and observing the peak shift on the spectrum measured using different circular-polarized photons is possible. Another approach is to measure the magnetic moment of the excited chiral phonon using circular-polarized photons, which can be applicable regardless of the presence of energy splitting. Light-induced demagnetization has been observed in many materials, including bulk  $\text{CrI}_3$  [79], due

to electronic excitation of crystal field levels. However, by adjusting the energy of photons to resonate with a chiral phonon but not to excite electrons, one can selectively probe the chiral phonons because the energy differences between crystal field levels or semicore levels are typically larger than phonon energies. Therefore, electronic excitations can be avoided when probing chiral phonons selectively.

## VI. CONCLUSION

Based on a Lagrangian formulation, we developed a theoretical formalism and computational methodology to determine adiabatic dynamics in systems with multiple slow degrees of freedom. Our computational methodology is based on static constrained DFT calculations of Hessians and Berry curvatures with respect to the slow parameters in order to extract the semiclassical dynamics. This constitutes a general and computationally efficient approach that does not require explicit time-dependent *ab initio* calculations as in, e.g., TDDFT, or other specialized capabilities beyond those commonly found in, or easily added to, widely available DFT codes. We demonstrate the utility of this methodology by applying it to phonons and spins (magnons) in magnetic insulators, as the dynamics of each is generally on the same energy scale. This represents a more systematic way of treating spin-phonon dynamics compared to conventional approaches which rely on building spin models and parameterizing their dependence on atomic displacements.

Specifically, we showed that the inclusion of the Hessians and Berry curvatures involving spin and phonon DOF are required to accurately describe the often-neglected effects of TRS breaking on phonon modes at the zone center. Results for four case-study materials were presented, covering both FM and AFM ordering, as well as 2D and 3D materials. FM  $\text{CrI}_3$  (both 3D bulk and 2D monolayer) exhibits energy splittings of its  $E$ -type modes (which are doubly degenerate under TRS) at the zone center. This results in chiral phonons exhibiting circular atomic motion leading to a significant phonon angular momentum. In AFM  $\text{Cr}_2\text{O}_3$  (3D bulk) and  $\text{VPSe}_3$  (2D monolayer), the  $E$ -type modes remain doubly degenerate, but the inversion symmetry breaking from the magnetic order results in modes with mixed  $E_g$  and  $E_u$  character. The angular momentum of a phonon in these materials is zero in total, but can exhibit well-defined nonzero *atom-resolved* contributions. In addition, the mixing of  $E_g$  and  $E_u$  modes implies that the Raman modes acquire some small IR character and vice versa, a feature that is open to experimental confirmation.

This work opens up various directions for future study. The general methodology will be useful in any material with interesting dynamics involving multiple slow DOF. Specifically in the area of spin-phonon dynam-

ics, it allows the search for materials with large splittings of chiral modes, due for example to large SOC or approximate degeneracies between phonon and magnon branches. It also motivates the exploration of dynamics of materials with more complicated magnetic structures, such as noncollinear or so-called altermagnetic [80, 81] orders. Finally, we focus here on zone-center modes, but the methodology shows promise for being generalized for computing the coupled spin-phonon dynamics across the Brillouin zone, which is relevant for the thermal Hall effect.

Overall, we expect that the developments in this work will allow efficient and accurate calculations of generalized adiabatic dynamics, and thus the exploration of much resulting novel physical phenomena, in spin-phonon coupled systems and beyond.

## ACKNOWLEDGMENTS

This work was supported by NSF Grant DMR-1954856 (D.V.) and Grant No. DMR-2237674 (C.E.D). M.S. acknowledges support from Ministerio de Ciencia e Innovación (MCIN/AEI/10.13039/501100011033) through Grant No. PID2019-108573GB-C22; from Severo Ochoa FUNFUTURE center of excellence (CEX2019-000917-S); from Generalitat de Catalunya (Grant No. 2021 SGR 01519); and from the European Research Council (ERC) under the European Union’s Horizon 2020 research and innovation program (Grant Agreement No. 724529). The authors thank Sinisa Coh for helpful discussions in the early stage of this work. S.R. and D.V. acknowledge the valuable discussions with Girsh Blumberg and Shangfei Wu, as well as their kind permission to reference their unpublished Raman measurement data. S.R. acknowledges the support of Predoctoral Researcher Program of Center for Computational Quantum Physics at the Flatiron Institute. The Flatiron Institute is a division of the Simons Foundation.

## Appendix A: Derivation of phonon Hamiltonian

In this section, we will review the adiabatic theory of phonons with TRS breaking, which is based on a Hamiltonian formalism first introduced by Mead and Truhlar (MT) [25]. In the MT approach, the only slow variables are nuclear coordinates. One can start from the full Hamiltonian for a system with electrons and nuclei, which is [82]

$$\begin{aligned} H_{\text{tot}} &= T_{\text{N}}(R) + T_{\text{e}}(r) + V(r, R), \\ T_{\text{N}}(R) &= - \sum_I \frac{\hbar^2 \nabla_I^2}{2M_I}, \\ T_{\text{e}}(r) &= - \sum_i \frac{\hbar^2 \nabla_i^2}{2m}, \end{aligned} \quad (\text{A1})$$

where  $T_{\text{N}}(R)$  and  $T_{\text{e}}(r)$  are nuclear kinetic energy and electronic kinetic energy, respectively.  $V(r, R)$  represents the total electrostatic interactions between electrons, nuclei, and electron-nuclei interactions, which includes the effects of spin-orbit coupling.  $R$  is the nuclear coordinate, and  $r$  is electronic.  $I$  runs over nuclei, and  $i$  runs over electrons.  $Z_{Ie}$  is the positive charge for the nucleus  $I$ . The Schrödinger equation for the wave function  $\Psi(r, R)$  is

$$[T_{\text{N}}(R) + T_{\text{e}}(r) + V(r, R)]\Psi(r, R) = W\Psi(r, R) \quad (\text{A2})$$

where  $W$  is the energy for the whole system.

Now one can implement the Born-Oppenheimer approximation [24], which treats  $R$  as a slow variable and assumes the electronic dynamics is always much faster than nuclear vibrations. As a consequence, the wave function can be separated to electronic and nuclear part

$$\Psi(r, R) = \psi(r; R)\chi(R), \quad (\text{A3})$$

where the electronic part  $\psi(r; R)$ , which satisfies

$$[T_{\text{e}}(r) + V(r, R)]\psi(r; R) = \epsilon(R)\psi(r; R), \quad (\text{A4})$$

is the normalized ground state wave function with respect to the nuclear coordinates  $R$ .  $\psi(r; R)$ ,  $V(r, R)$  and  $\epsilon(R)$  depends on  $R$  parametrically. One should also notice that  $\psi(r; R)$  has a  $U(1)$  gauge freedom, namely

$$\tilde{\psi}(r; R) = e^{i\phi(R)}\psi(r; R) \quad (\text{A5})$$

is also a solution to Eq. (A4), where  $e^{i\phi(R)}$  is an  $R$ -dependent phase factor. Plugging Eq. (A3) into Eq. (A2), multiplying  $\psi^*(r; R)$  from the left, and integrating over  $r$ , gives

$$\begin{aligned} \left[ \sum_{I\alpha} \frac{(P_{I\alpha} - \hbar A_{I\alpha})^2}{2M_I} + \epsilon(R) + \Lambda(R) \right] \chi(R) &= W\chi(R), \\ \Lambda(R) &= \frac{\hbar^2}{2M_I} (\langle \partial_{I\alpha} \psi(R) | \partial_{I\alpha} \psi(R) \rangle - A_{I\alpha}^2), \\ A_{I\alpha} &= i \langle \psi(R) | \partial_{I\alpha} \psi(R) \rangle, \end{aligned} \quad (\text{A6})$$

where  $A_{I\alpha}$  is a Berry potential with respect to nuclear displacements thus called “nuclear Berry potential”. As first pointed out by Mead and Truhlar [25], it is not always possible to make  $A_{I\alpha}$  zero by tuning the  $R$ -dependent phase  $\phi(R)$  in Eq. (A5). Here the Dirac bracket notation is only for the electronic degree of freedom  $r$ . Note that  $\Lambda(R)$  can be rewritten as

$$\begin{aligned} \Lambda(R) &= \frac{\hbar^2}{2M_I} \langle \partial_{I\alpha} \psi(R) | Q | \partial_{I\alpha} \psi(R) \rangle, \\ Q &= 1 - |\psi(R)\rangle\langle\psi(R)|, \end{aligned} \quad (\text{A7})$$

therefore  $\Lambda(R)$  is gauge-independent.  $\Lambda(R)$  is related to the expectation value of electronic kinetic energy  $\langle T_{\text{e}}(r) \rangle$  to the order of  $m/M$ , where  $m$  and  $M$  are electronic and nuclear mass, respectively. As  $\langle T_{\text{e}}(r) \rangle$  is included in  $\epsilon(R)$ ,



we have  $\Lambda(R) \ll \epsilon(R)$ . Since we focus on broken time-reversal symmetry (TRS) in this work, it is worth noting that  $\Lambda(R)$  does not break TRS. Therefore, we disregard  $\Lambda(R)$  in this work. In addition, we only consider nuclear DOF in this section. To simplify the notation, we introduce a composite index  $l$  for  $I\alpha$ , which is used to label nuclear DOF.

Now we are ready to write down the effective Hamiltonian for phonons, which is

$$H_{\text{eff}} = \sum_l \frac{(P_l - \hbar A_l)^2}{2M_l} + \epsilon(R), \quad (\text{A8})$$

and the equation of motion (EOM) is

$$\dot{R}_l = \frac{\partial H}{\partial P_l} = \frac{P_l - \hbar A_l}{M_l}, \quad (\text{A9})$$

$$\begin{aligned} \dot{P}_l &= -\frac{\partial H}{\partial R_l} = \sum_m \frac{P_m - \hbar A_m}{M_m} (\partial_l A_m) - \partial_l \epsilon(R), \\ &= \hbar \sum_m \dot{R}_m \partial_l A_m - \partial_l \epsilon(R), \end{aligned} \quad (\text{A10})$$

where  $\partial_l$  denotes  $\partial/\partial R_l$ . Combining Eq. (A10) and Eq. (A9), one can get

$$\begin{aligned} M_l \ddot{R}_l &= \dot{P}_l - \hbar \dot{A}_l \\ &= -\partial_l \epsilon(R) + \hbar \sum_m \dot{R}_m (\partial_l A_m - \partial_m A_l), \end{aligned} \quad (\text{A11})$$

where we have used the relation  $\dot{A}_l(R) = (\partial_m A_l) \dot{R}_m$  in the second line. By introducing

$$G_{lm} = \hbar \Omega_{lm} = \hbar (\partial_l A_m - \partial_m A_l), \quad (\text{A12})$$

where the  $\Omega_{lm}$  is the nuclear Berry curvature, which is gauge-invariant, Eq. (A11) can be written in a compact form as

$$M_l \ddot{R}_l = -\partial_l \epsilon(R) + \sum_m G_{lm}(R) \dot{R}_m. \quad (\text{A13})$$

Equation (A13) is equivalent to Eq. (9) for the case that  $Q_i$  corresponds to a nuclear DOF. However, they are obtained using Hamiltonian and Lagrangian formalism, respectively. In this way, starting with a full quantum theory, a semiclassical theory of the dynamics has been derived.

## Appendix B: From present approach to spin-phonon model

It has been mentioned in Sec. II C that the spin-phonon model in Ref. [33] only includes  $G^{(\text{ss})}$  and neglects all other Berry curvature tensors, which we shall illustrate below. If we let  $G^{(\text{pp})}$ ,  $G^{(\text{ps})}$  and  $G^{(\text{sp})}$  be all zero, then we get the EOM for the spin-phonon model as

$$\begin{aligned} M^{(\text{pp})} |\ddot{u}\rangle &= -K^{(\text{pp})} |u\rangle - K^{(\text{ps})} |s\rangle, \\ G^{(\text{ss})} |\dot{s}\rangle &= K^{(\text{sp})} |u\rangle + K^{(\text{ss})} |s\rangle. \end{aligned} \quad (\text{B1})$$

These equations can be solved exactly. However, to establish a connection with the minimal spin-phonon model proposed in Ref. [33], we can derive Eq. (6) in that reference from Eq. (B1).

We introduce the new phonon vector  $|v\rangle = M^{1/2} |u\rangle$ , so that  $M^{(\text{pp})}$  no longer appears in the EOM explicitly. Consequently, Eq. (B1) can be rewritten as

$$|\ddot{v}\rangle = -\tilde{K}^{(\text{pp})} |v\rangle - \tilde{K}^{(\text{ps})} |s\rangle, \quad (\text{B2})$$

$$G^{(\text{ss})} |\dot{s}\rangle = \tilde{K}^{(\text{sp})} |v\rangle + K^{(\text{ss})} |s\rangle, \quad (\text{B3})$$

where  $\tilde{K}^{(\text{pp})} = [M^{(\text{pp})}]^{-1/2} K^{(\text{pp})} [M^{(\text{pp})}]^{-1/2}$ ,  $\tilde{K}^{(\text{ps})} = [M^{(\text{pp})}]^{-1/2} K^{(\text{ps})}$ , and  $\tilde{K}^{(\text{sp})} = K^{(\text{sp})} [M^{(\text{pp})}]^{-1/2}$ . Note that  $\tilde{K}^{(\text{pp})}$  is the dynamical matrix.

Now we only focus on bulk  $\text{CrI}_3$ , and include one bare phonon doublet and the magnon from the same irrep in the formalism. We introduce the unperturbed solution of Eqs. (B2) and (B3), which we referred to as bare phonons and magnons, as

$$\tilde{K}^{(\text{pp})} |v_{\pm}\rangle = \omega_p^2 |v_{\pm}\rangle, \quad (\text{B4})$$

$$K^{(\text{ss})} |s_{\pm}\rangle = -i\omega_m G^{(\text{ss})} |s_{\pm}\rangle, \quad (\text{B5})$$

where  $\omega_p$  and  $\omega_m$  are energies for bare phonons and magnons, respectively. The  $\pm$  subscript in  $|v_{\pm}\rangle$  and  $|s_{\pm}\rangle$  represents the left and right-hand circular polarized modes. Specifically, for the  $E_g$  magnon, we have  $|s_{\pm}\rangle = \frac{1}{2}(1, \mp i, 1, \mp i)^T$ , where the first two components correspond to the  $x$  and  $y$  components of the reduced spin unit vector of the first Cr atom, and the last two components correspond to the second Cr atom. Similarly, for the  $E_u$  magnon, we have  $|s_{\pm}\rangle = \frac{1}{2}(1, \mp i, -1, \pm i)^T$ .

If we adopt the assumption made in Ref.[33], which states that

$$G = -S \begin{pmatrix} 0 & 1 & 0 & 0 \\ -1 & 0 & 0 & 0 \\ 0 & 0 & 0 & 1 \\ 0 & 0 & -1 & 0 \end{pmatrix}, \quad (\text{B6})$$

we can verify that

$$\langle s_{\pm} | G^{(\text{ss})} | s_{\pm} \rangle = \pm i S, \quad (\text{B7})$$

regardless of whether  $|s_{\pm}\rangle$  belongs to the  $E_g$  or  $E_u$  magnons. However, in our numerical calculations for  $\text{CrI}_3$ , we have observed that the effective spin  $S$  for  $E_g$  and  $E_u$  magnons is slightly different. The numerical values for these effective spins are provided in Appendix C.

According to symmetry considerations, modes with different chiralities should not mix under any of the matrices in Eq. (B1). Therefore, we have

$$\langle s_{\pm} | K^{(\text{sp})} | v_{\pm} \rangle = \gamma, \quad (\text{B8})$$

$$\langle s_{\pm} | K^{(\text{sp})} | v_{\mp} \rangle = 0, \quad (\text{B9})$$

where  $\gamma$  represents the spin-phonon coupling strength. It is always possible to add a phase to either  $|s_{\pm}\rangle$  or  $|v_{\pm}\rangle$

in order to make  $\gamma$  real. Therefore, we assume  $\gamma$  to be real, resulting in  $\langle s_{\pm} | K^{(\text{sp})} | v_{\pm} \rangle = \langle v_{\pm} | K^{(\text{ps})} | s_{\pm} \rangle = \gamma$ .

We can expand  $|v\rangle$  and  $|s\rangle$  in the bases of  $|v_{\pm}\rangle$  and  $|s_{\pm}\rangle$  as

$$|v\rangle = x_{\pm}|v_{\pm}\rangle, \quad (\text{B10})$$

$$|s\rangle = s_{\pm}|s_{\pm}\rangle, \quad (\text{B11})$$

where  $x_{\pm}$  and  $s_{\pm}$  are coefficients representing the magnitudes of the contributions from the corresponding basis vectors. In the minimal spin-phonon model, it is assumed that the mixing between different  $E_g$  doublets is negligible. However, in reality, this mixing, which is mediated by magnons, plays a crucial role in explaining why the angular momenta of the two circular polarized modes do not cancel out exactly. A more detailed analysis of this mixing based on the perturbation approach can be found in Appendix D 1.

By multiplying  $\langle v_{\pm} |$  to Eq. (B2) and substituting Eqs.(B4), (B10), and (B8), we obtain

$$(\omega_p^2 - \omega^2)x_{\pm} = -\gamma s_{\pm}. \quad (\text{B12})$$

Similarly, by multiplying  $\langle s_{\pm} |$  to Eq. (B3) and substituting Eqs.(B5), (B7), and (B8), we get

$$(\pm\omega_s - \omega)s_{\pm} = \mp S^{-1}\gamma x_{\pm}. \quad (\text{B13})$$

Thus, we have successfully derived Eq. (6) in Ref. [33].

Although Eq. (B1) is derived from an adiabatic Lagrangian formalism, we aim to demonstrate that it can also emerge from the undamped Landau-Lifshitz equation [52]. In its original form, the Landau-Lifshitz equation is presented as

$$\frac{d\vec{M}}{dt} = -\gamma\vec{M} \times \frac{dH}{d\vec{M}}, \quad (\text{B14})$$

where  $H$  is the Hamiltonian,  $dH/d\vec{M}$  is the effective magnetic field, and  $\gamma$  represents the gyromagnetic ratio, which is the ratio of the magnetic moment  $\vec{M}$  to its corresponding angular momentum  $\vec{S}$ . As the dynamic variable in our study is the unit vector of spin,  $\vec{s} = \vec{S}/S$ , we can recast Eq. (B14) in terms of  $\vec{s}$  as

$$S \frac{d\vec{s}}{dt} = -\vec{s} \times \frac{dH}{d\vec{s}}. \quad (\text{B15})$$

Equation (B15) can be rewritten in component form as

$$S \frac{ds_{\alpha}}{dt} = -\epsilon_{\alpha\beta\gamma} s_{\beta} \frac{dH}{ds_{\gamma}}, \quad (\text{B16})$$

where  $\alpha$ ,  $\beta$ , and  $\gamma$  span over the Cartesian coordinates. Given that the spin deviation from the  $z$ -direction is small, we can make a simplification on the right-hand side of this equation by setting  $\beta = z$ . Consequently, the equation transforms to

$$S \frac{ds_{\alpha}}{dt} = \epsilon_{\alpha\gamma} \frac{dH}{ds_{\gamma}}, \quad (\text{B17})$$

where now,  $\alpha$  and  $\gamma$  are confined to  $x$  and  $y$  Cartesian directions. By reintroducing the matrix form and transferring the  $\epsilon$  tensor to the left-hand side, we arrive at

$$-S\epsilon \frac{d\vec{s}}{dt} = \frac{dH}{d\vec{s}}. \quad (\text{B18})$$

Referring back to Eq. (B6), it is noteworthy that  $-S\epsilon$  is equivalent to the  $G^{(\text{ss})}$ . Since the Hamiltonian has been expanded up to the quadratic order, the derivative  $dH/d\vec{s}$  can be expressed as

$$\frac{dH}{d\vec{s}} = K^{(\text{ss})}|s\rangle + K^{(\text{sp})}|u\rangle, \quad (\text{B19})$$

where we have chosen to use the bra-ket notation for ease of representation. This gives rise to

$$G^{(\text{ss})}|s\rangle = K^{(\text{ss})}|s\rangle + K^{(\text{sp})}|u\rangle, \quad (\text{B20})$$

which aligns with the form presented in Eq. (B1). Thus, we have successfully shown the equivalence of the EOM for the spin-phonon model presented in this Appendix with the undamped Landau-Lifshitz equation.

### Appendix C: Spin-spin Hessians ( $K^{(\text{ss})}$ ) and Berry curvatures ( $\Omega^{(\text{ss})}$ ) for all four materials

In this appendix, we present the spin-spin Hessians and Berry curvatures for all four materials investigated in our study.

For bulk  $\text{CrI}_3$ , both the spin-spin Hessian ( $K^{(\text{ss})}$ ) and Berry curvature ( $\Omega^{(\text{ss})}$ ) matrices have the form

$$M_{4 \times 4} = \begin{pmatrix} a & b \\ b & a \end{pmatrix}, \quad (\text{C1})$$

where both  $a$  and  $b$  are  $2 \times 2$  matrices that are restricted to be of the form

$$a = a_{\text{sym}} \begin{pmatrix} 1 & 0 \\ 0 & 1 \end{pmatrix} + a_{\text{asym}} \begin{pmatrix} 0 & 1 \\ -1 & 0 \end{pmatrix}, \quad (\text{C2})$$

and similarly for  $b$ , as a result of the three-fold symmetry. In Table XI we provide the symmetric and antisymmetric parts of  $a$  and  $b$  for both  $K^{(\text{ss})}$  and  $\Omega^{(\text{ss})}$  of bulk  $\text{CrI}_3$ . It is noteworthy that the eigenvalues of  $\Omega^{(\text{ss})}$  are 1.499 and 1.566 for the  $E_g$  and  $E_u$  modes, respectively. These values represent the effective spins of the respective magnon modes. They are close to  $3/2$  as expected from the nominal spin of the  $\text{Cr}^{3+}$  ion, but they do differ slightly, especially for the optical  $E_u$  magnon. Instead, the deviation is very small for the acoustic  $E_g$  magnon. These deviations were not captured by the minimal spin-phonon model proposed in Ref. [33].

The symmetry-allowed matrix elements for monolayer  $\text{CrI}_3$  exhibit a similar structure to those of bulk  $\text{CrI}_3$ , and they can also be decomposed following the same procedure as described in Eqs. (C1) and (C2). The numerical values of these matrix elements are provided in Table XI.

TABLE XI. Matrix elements  $K^{(ss)}$  and  $\Omega^{(ss)}$  for materials under study (ML = monolayer). Symmetric ('sym') and antisymmetric ('asym') parts are defined in Eq. (C2). For  $\Omega^{(ss)}$  of  $\text{Cr}_2\text{O}_3$ , the values of  $c_{\text{sym}} = -6.211 \times 10^{-5}$  and  $d_{\text{sym}} = -2.409 \times 10^{-4}$  appear rounded to zero.

Material	Term	$K^{(ss)}$ (meV)		$\Omega^{(ss)}$	
		sym	asym	sym	asym
CrI <sub>3</sub>	a	18.340	0	0	-1.533
	b	-17.455	0	0	0.033
ML CrI <sub>3</sub>	a	8.956	0	0	-1.526
	b	-7.497	0	0	0.026
Cr <sub>2</sub> O <sub>3</sub>	a	72.182	0	0	-1.454
	b	17.360	0.082	0	0
	c	-27.193	1.275	0.000	0.023
	d	27.479	0	0.000	0
ML VPSe <sub>3</sub>	a	143.092	0	0	-1.351
	b	142.622	0	0	0

For bulk  $\text{Cr}_2\text{O}_3$ , the non-zero matrix elements of  $K^{(ss)}$  are given by

$$K^{(ss)} = \begin{pmatrix} a & b & c & d \\ b^T & a^T & d & c^T \\ c^T & d^T & a & b^T \\ d^T & c & b & a^T \end{pmatrix}, \quad (\text{C3})$$

while the non-zero matrix elements of  $G^{(ss)}$  are

$$G^{(ss)} = \begin{pmatrix} a & b & c & d \\ -b^T & a^T & d & c^T \\ -c^T & -d^T & a & b^T \\ -d^T & -c & -b & a^T \end{pmatrix}, \quad (\text{C4})$$

Here,  $a$ ,  $b$ ,  $c$ , and  $d$  can also be decomposed in the same manner as in Eq. (C2). The numerical results for these matrix elements are provided in Table XI.

For monolayer VPSe<sub>3</sub>, the matrix elements of both  $K^{(ss)}$  and  $\Omega^{(ss)}$  have the form

$$M_{4 \times 4} = \begin{pmatrix} a & b \\ b & a^T \end{pmatrix}, \quad (\text{C5})$$

where  $a$  and  $b$  are  $2 \times 2$  matrices. The values of these matrix elements can be found in Table XI.

From Table XI we can find that, for the systems with at most two spins, the asymmetric (symmetric) parts of  $K^{(ss)}$  ( $G^{(ss)}$ ) all vanish. However, the symmetry is more complicated in  $\text{Cr}_2\text{O}_3$ , where some of the  $b$ ,  $c$ , and  $d$  components in Eqs. (C3) and (C4) have both symmetric and asymmetric components.

#### Appendix D: Perturbation treatment of phonon-magnon dynamics

In the main text, we have directly solved the equation of motion (EOM) of the present approach (Eq. (10)). However, employing perturbation theory to solve the

EOM can offer valuable physical insights into the influence of Hessian matrices and Berry curvatures on the results. In this section, we will present a perturbation treatment for  $K^{(sp)}$ ,  $G^{(ps)}$ , and  $G^{(pp)}$  individually. Furthermore, we will provide numerical results from the perturbation treatment of  $K^{(sp)}$  and compare them with the predictions of the spin-phonon model.

We begin by reformulating Eq. (10) in matrix form as

$$(K + i\omega_i G - \omega_i^2 M)|q_i\rangle = 0, \quad (\text{D1})$$

where the matrices  $M$ ,  $K$ , and  $G$  are defined in Eq. (11). At variance with the main text, in this Appendix we let  $i, j$  label mixed modes, while  $m, n$  and  $\mu, \nu$  label bare phonon and bare magnon modes respectively. We utilize the bare phonon and magnon states  $|u_n^{(0)}\rangle$  and  $|s_\mu^{(0)}\rangle$  as the basis functions for the perturbation theory, where the superscript '(0)' denotes the zeroth order in the perturbation expansion.

The EOM for unperturbed phonons can be expressed in matrix form as

$$(K^{(pp)} - \xi_n M^{(pp)})|u_n^{(0)}\rangle = 0 \quad (\text{D2})$$

where for convenience we have introduced the squared frequency  $\xi_n = \omega_n^2$ , and for the magnons as

$$(K^{(ss)} + i\omega_\mu G^{(ss)})|s_\mu^{(0)}\rangle = 0, \quad (\text{D3})$$

where  $\omega_\mu$  may be positive or negative even though solutions with negative energy are not physically observable. The fact that  $\langle u_m^{(0)} | M^{(pp)} | u_n^{(0)} \rangle = 0$  for  $\xi_m \neq \xi_n$  and that  $\langle s_\mu^{(0)} | G^{(ss)} | s_\nu^{(0)} \rangle = 0$  for  $\omega_\mu \neq \omega_\nu$  allows us to adopt the normalization conditions

$$\langle u_m^{(0)} | M^{(pp)} | u_n^{(0)} \rangle = \delta_{mn}, \quad (\text{D4})$$

$$\langle s_\mu^{(0)} | iG^{(ss)} | s_\nu^{(0)} \rangle = \delta_{\mu\nu} \sigma_\mu, \quad (\text{D5})$$

where  $\sigma_\mu$  takes the values  $\mp 1$  for  $\omega_\mu > 0$  and  $\omega_\mu < 0$  respectively. The solution to Eq. (D1) is a composite vector that includes both the phonon and magnon sectors, living in the space spanned by basis vectors  $|u_n^{(0)}\rangle \oplus |0\rangle$  and  $|0\rangle \oplus |s_\mu^{(0)}\rangle$ .

As discussed in the main text, phonons and magnons belonging to the  $E$  irreducible representations can be doubly degenerate. To address this, we need to employ degenerate perturbation theory. However, we can simplify the analysis by considering the '+' and '-' sectors separately. Phonons and magnons from different sectors do not mix, allowing us to work with these bases throughout this section.

##### 1. Perturbation treatment of $K^{(sp)}$

We begin by examining the perturbation of  $K^{(sp)}$  alone, neglecting  $G^{(pp)}$  and  $G^{(sp)}$ . We replace  $K^{(sp)}$  with

$\lambda K^{(\text{sp})}$ , where  $\lambda$  serves as our perturbation parameter, and expand Eq. (D1) up to second order in  $\lambda$  as

$$\begin{aligned} K &= K^{(0)} + \lambda K^{(1)}, \\ K^{(0)} &= \begin{pmatrix} K^{(\text{pp})} & 0 \\ 0 & K^{(\text{ss})} \end{pmatrix}, \\ K^{(1)} &= \begin{pmatrix} 0 & K^{(\text{ps})} \\ K^{(\text{sp})} & 0 \end{pmatrix}, \\ \omega_i &= \omega_i^{(0)} + \lambda \omega_i^{(1)} + \lambda^2 \omega_i^{(2)} + \dots, \\ \xi_i &= \xi_i^{(0)} + \lambda \xi_i^{(1)} + \lambda^2 \xi_i^{(2)} + \dots, \\ |q_i\rangle &= |q_i^{(0)}\rangle + \lambda |q_i^{(1)}\rangle + \lambda^2 |q_i^{(2)}\rangle + \dots \end{aligned} \quad (\text{D6})$$

We substitute these equations into Eq. (D1) and expand in orders of  $\lambda$ , making use of the relations

$$\begin{aligned} \xi_i^{(0)} &= (\omega_i^{(0)})^2, \\ \xi_i^{(1)} &= 2\omega_i^{(0)}\omega_i^{(1)}, \\ \xi_i^{(2)} &= (\omega_i^{(1)})^2 + 2\omega_i^{(0)}\omega_i^{(2)}. \end{aligned} \quad (\text{D7})$$

At zero order this yields

$$(K^{(0)} + i\omega_i^{(0)}G - \xi_i^{(0)}M)|q_i^{(0)}\rangle = 0, \quad (\text{D8})$$

which corresponds to the EOM for decoupled phonons and magnons.

The equation at first order in  $\lambda$  is

$$\begin{aligned} (K^{(0)} + i\omega_i^{(0)}G - \xi_i^{(0)}M)|q_i^{(1)}\rangle \\ + (K^{(1)} + i\omega_i^{(1)}G - \xi_i^{(1)}M)|q_i^{(0)}\rangle = 0. \end{aligned} \quad (\text{D9})$$

Multiplying Eq. (D9) on the left by  $\langle q_i^{(0)}|$ , noting that  $\langle q_i^{(0)}|(K^{(0)} + i\omega_i^{(0)}G - \xi_i^{(0)}M) = 0$ , and also that  $\langle q_i^{(0)}|K^{(1)}|q_i^{(0)}\rangle = 0$  since  $K^{(1)}$  is block-off-diagonal in the phonon and magnon DOF, we obtain

$$\omega_i^{(1)} \left( \langle q_i^{(0)}|iG|q_i^{(0)}\rangle - 2\omega_i^{(0)}\langle q_i^{(0)}|M|q_i^{(0)}\rangle \right) = 0, \quad (\text{D10})$$

which indicates that  $\omega_i^{(1)} = 0$ , so that also  $\xi_i^{(1)} = 0$ . This is similar to the perturbation theory in quantum mechanics, where the first-order energy correction is always given by the diagonal matrix element of the interaction Hamiltonian, which is zero in our case.

To obtain  $|q_i^{(1)}\rangle$ , we multiply Eq. (D9) by  $\langle q_j^{(0)}|$  on the left and use  $\omega_i^{(1)} = \xi_i^{(1)} = 0$ . This gives

$$\langle q_j^{(0)}|K^{(0)} + i\omega_i^{(0)}G - \xi_i^{(0)}M|q_i^{(1)}\rangle + \langle q_j^{(0)}|K^{(1)}|q_i^{(0)}\rangle = 0. \quad (\text{D11})$$

We observe that if  $i$  and  $j$  both label phonons or both label magnons,  $K^{(1)}$  has no effect. Therefore,  $|q_n^{(1)}\rangle$  for phonons has a pure magnon character, and  $|q_\mu^{(1)}\rangle$  for magnons has a pure phonon character.

### a. Perturbation of phonons

We focus on the perturbation for phonons first, and we replace  $|q_i\rangle$  and  $|q_j\rangle$  in Eq. (D11) with  $|u_n\rangle$  and  $|s_\mu\rangle$ , respectively. Then Eq. (D11) becomes

$$\langle s_\mu^{(0)}|K^{(0)} + i\omega_n^{(0)}G - \xi_n^{(0)}M|u_n^{(1)}\rangle + \langle s_\mu^{(0)}|K^{(\text{sp})}|u_n^{(0)}\rangle = 0. \quad (\text{D12})$$

To obtain  $|u_n^{(1)}\rangle$ , we expand it in terms of the basis  $|s_\nu^{(0)}\rangle$  as

$$|u_n^{(1)}\rangle = \sum_\nu c_{\nu n}^{(1)}|s_\nu^{(0)}\rangle. \quad (\text{D13})$$

Substituting Eq. (D13) into Eq. (D12), we have

$$\sum_\nu c_{\nu n}^{(1)} \langle s_\mu^{(0)}|K^{(\text{ss})} + i\omega_n^{(0)}G^{(\text{ss})}|s_\nu^{(0)}\rangle + \langle s_\mu^{(0)}|K^{(\text{sp})}|u_n^{(0)}\rangle = 0. \quad (\text{D14})$$

Using the relation  $(K^{(\text{ss})} + i\omega_n^{(0)}G^{(\text{ss})})|s_\nu^{(0)}\rangle = 0$ , we find

$$\begin{aligned} \sum_\nu c_{\nu n}^{(1)} \omega_{n\nu}^{(0)} \langle s_\mu^{(0)}|iG^{(\text{ss})}|s_\nu^{(0)}\rangle + \langle s_\mu^{(0)}|K^{(\text{sp})}|u_n^{(0)}\rangle \\ = c_{\mu n}^{(1)} \omega_{n\mu}^{(0)} \sigma_\mu + \langle s_\mu^{(0)}|K^{(\text{sp})}|u_n^{(0)}\rangle = 0, \end{aligned} \quad (\text{D15})$$

where  $\omega_{n\mu}^{(0)}$  denotes  $\omega_n^{(0)} - \omega_\mu^{(0)}$ . Using Eq. (D15), we can determine  $c_{\mu n}^{(1)}$  and express  $|u_n^{(1)}\rangle$  as

$$|u_n^{(1)}\rangle = \sum_\mu \sigma_\mu \frac{\langle s_\mu^{(0)}|K^{(\text{sp})}|u_n^{(0)}\rangle}{\omega_\mu^{(0)} - \omega_n^{(0)}} |s_\mu^{(0)}\rangle. \quad (\text{D16})$$

This is the first major result of this Appendix. It is worth noting that the first-order perturbation of the phonons only has spin character, so that the phonon character remains unchanged. This cannot explain why the angular momentum summed over a pair of  $E_g$  or  $E_u$  chiral phonons is not zero, as can be seen in Tables I and VIII of the main text. To explain this effect, we need to consider the second-order perturbation.

Since we have seen that the first-order correction  $\omega_n^{(1)}$  to the phonon energy vanishes, we need to calculate the second-order correction  $\omega_n^{(2)}$  in order to determine the energy splitting of the chiral phonons. By expanding Eq. (D1) to the second order in  $\lambda$ , we obtain

$$\begin{aligned} (K^{(0)} + i\omega_i^{(0)}G - \xi_i^{(0)}M)|q_i^{(2)}\rangle + K^{(1)}|q_i^{(1)}\rangle \\ + (i\omega_i^{(2)}G - \xi_i^{(2)}M)|q_i^{(0)}\rangle = 0. \end{aligned} \quad (\text{D17})$$

Multiplying Eq. (D17) by  $\langle q_i^{(0)}|$  from the left, we obtain

$$\langle q_i^{(0)}|K^{(1)}|q_i^{(1)}\rangle + \langle q_i^{(0)}|i\omega_i^{(2)}G - \xi_i^{(2)}M|q_i^{(0)}\rangle = 0. \quad (\text{D18})$$

For phonons, we replace  $|q_i\rangle$  with  $|u_n\rangle$  and substitute Eq. (D16) into Eq. (D18), yielding

$$\xi_n^{(2)} = \sum_\mu \sigma_\mu \frac{|\langle s_\mu^{(0)}|K^{(\text{sp})}|u_n^{(0)}\rangle|^2}{\omega_\mu^{(0)} - \omega_n^{(0)}} \quad (\text{D19})$$



or equivalently

$$\omega_n^{(2)} = \sum_{\mu} \sigma_{\mu} \frac{|\langle s_{\mu}^{(0)} | K^{(\text{sp})} | u_n^{(0)} \rangle|^2}{2\omega_n^{(0)}(\omega_{\mu}^{(0)} - \omega_n^{(0)})}. \quad (\text{D20})$$

This is a second major result. The summation over  $\mu$  in Eqs. (D16) and (D20) runs over all solutions of Eq. (D3), including those of negative energy. Thus, the unphysical negative-energy states can still contribute to the perturbation of the phonons. It is worth noting that Eq. (D20) explains why phonons from the ‘+’ sector exhibit larger energy splitting. Since positive-energy magnons also belong to the ‘+’ sector, the interactions between magnons and phonons are stronger in the ‘+’ sector due to the smaller energy denominator.

Furthermore, we can obtain  $|u_n^{(2)}\rangle$  by left-multiplying Eq. (D17) with  $\langle q_j^{(0)}|$ . This yields

$$\begin{aligned} \langle q_j^{(0)} | K^{(0)} + i\omega_i^{(0)} G - \xi_i^{(0)} M | q_i^{(2)} \rangle + \langle q_j^{(0)} | K^{(1)} | q_i^{(1)} \rangle \\ + \langle q_j^{(0)} | i\omega_i^{(2)} G - \xi_i^{(2)} M | q_i^{(0)} \rangle = 0. \end{aligned} \quad (\text{D21})$$

If  $i$  labels a phonon and  $j$  labels a magnon, both the second and third terms in Eq. (D21) are zero, implying that the first term is also zero. It follows that  $|q_i^{(2)}\rangle$  can only possess phonon character. Replacing  $|q_i\rangle$  and  $|q_j\rangle$  by  $|u_n\rangle$  and  $|u_m\rangle$  and substituting Eq. (D16) into Eq. (D21) yields

$$|u_n^{(2)}\rangle = \sum_{m \neq n} \sum_{\mu} \sigma_{\mu} \frac{\langle u_m^{(0)} | K^{(\text{ps})} | s_{\mu}^{(0)} \rangle \langle s_{\mu}^{(0)} | K^{(\text{sp})} | u_n^{(0)} \rangle}{(\xi_n^{(0)} - \xi_m^{(0)})(\omega_{\mu}^{(0)} - \omega_n^{(0)})} |u_m^{(0)}\rangle, \quad (\text{D22})$$

which represents the effect of the magnon-mediated phonon-phonon interaction at second order. It provides an explanation for the non-canceling angular momentum observed in chiral phonon pairs, as shown in Table I and VIII.

### b. Perturbation of magnons

We now turn to the corresponding perturbation treatment of the magnons. First, we replace  $|q_i\rangle$  and  $|q_j\rangle$  in Eq. (D11) with  $|s_{\mu}\rangle$  and  $|u_n\rangle$ , respectively. Then, we multiply Eq. (D11) by  $|u_n^{(0)}\rangle$  from the left, resulting in

$$\langle u_n^{(0)} | K^{(0)} + i\omega_{\mu}^{(0)} G - \xi_{\mu}^{(0)} M | s_{\mu}^{(1)} \rangle + \langle u_n^{(0)} | K^{(\text{ps})} | s_{\mu}^{(0)} \rangle = 0. \quad (\text{D23})$$

Next, we expand  $|s_{\mu}^{(1)}\rangle$  in terms of the basis of  $|u_m^{(0)}\rangle$  as

$$|s_{\mu}^{(1)}\rangle = \sum_m d_{m\mu}^{(1)} |u_m^{(0)}\rangle. \quad (\text{D24})$$

Substituting this expansion into Eq. (D23), we obtain

$$\begin{aligned} \sum_m d_{m\mu}^{(1)} \langle u_n^{(0)} | K^{(\text{pp})} - \xi_{\mu}^{(0)} M | u_m^{(0)} \rangle + \langle u_n^{(0)} | K^{(\text{ps})} | s_{\mu}^{(0)} \rangle \\ = -d_{n\mu}^{(1)} \xi_{\mu n} + \langle u_n^{(0)} | K^{(\text{ps})} | s_{\mu}^{(0)} \rangle = 0, \end{aligned} \quad (\text{D25})$$

TABLE XII. Comparison of perturbation approach and exact solution in the spin-phonon model. The perturbation approach provides second-order perturbations to phonon and magnon energies  $E_n^{(2)} = \hbar\omega_n^{(2)}$  and first-order perturbations to phonon states  $c_{\nu n}^{(1)}$ . The exact solutions for phonon and magnon energy shifts  $\Delta E = \hbar\Delta\omega$  and the spin component of phonon-like solutions  $c_{\nu n}$  are included as benchmarks. The bare phonon and magnon energies  $E_n^{(0)} = \hbar\omega_n^{(0)}$  are provided as reference values for energy perturbations or shifts.

Irrep	$E_n^{(0)}$ (meV)	$E_n^{(2)}$ ( $\mu\text{eV}$ )	$\Delta E$ ( $\mu\text{eV}$ )	$c_{\nu n}^{(1)}$ ( $10^{-3}$ )	$c_{\nu n}$ ( $10^{-3}$ )
Phonons					
$E_g$	7.000	-1.323	-1.324	1.562	1.563
		1.566	1.565	1.850	1.849
	12.929	-0.545	-0.545	1.021	1.021
		0.597	0.597	1.118	1.118
	13.488	-0.244	-0.244	0.684	0.683
		0.266	0.266	0.746	0.747
	29.852	-0.001	-0.001	0.050	0.050
		0.001	0.001	0.052	0.052
$E_u$	10.769	-4.431	-4.453	2.809	2.823
		-1.593	-1.597	1.010	1.012
	14.329	-17.563	-17.546	7.680	7.668
		-4.030	-4.031	1.762	1.763
	27.823	-3.506	-3.506	1.962	1.962
		35.836	35.623	20.053	19.947
Magnons					
$E_g$	0.590	-4.544	-4.543		
$E_u$	22.864	-22.971	-22.757		

From Eq. (D25), we can determine the coefficients  $d_{n\mu}^{(1)}$ . Therefore, the first-order perturbation of the magnons is given by

$$|s_{\mu}^{(1)}\rangle = \sum_n \frac{\langle u_n^{(0)} | K^{(\text{ps})} | s_{\mu}^{(0)} \rangle}{\xi_{\mu}^{(0)} - \xi_n^{(0)}} |u_n^{(0)}\rangle. \quad (\text{D26})$$

To get the second order energy perturbation for magnons, we replace  $|q_i\rangle$  with  $|s_{\mu}\rangle$  and substitute Eq. (D26) into Eq. (D18). This leads to

$$\omega_{\mu}^{(2)} = \sum_n \sigma_{\mu} \frac{|\langle u_n^{(0)} | K^{(\text{ps})} | s_{\mu}^{(0)} \rangle|^2}{\xi_n^{(0)} - \xi_{\mu}^{(0)}}. \quad (\text{D27})$$

The second order perturbation of the magnon states can be obtained in a similar way as was done for the phonons. We replace  $|q_i\rangle$  and  $|q_j\rangle$  with  $|s_{\mu}\rangle$  and  $|s_{\nu}\rangle$  and substitute Eq. (D26) into Eq. (D21). This substitution yields

$$|s_{\mu}^{(2)}\rangle = \sum_{\nu \neq \mu} \sum_n \sigma_{\nu} \frac{\langle s_{\nu}^{(0)} | K^{(\text{sp})} | u_n^{(0)} \rangle \langle u_n^{(0)} | K^{(\text{ps})} | s_{\mu}^{(0)} \rangle}{(\omega_{\mu}^{(0)} - \omega_{\nu}^{(0)})(\xi_n^{(0)} - \xi_{\mu}^{(0)})} |s_{\nu}^{(0)}\rangle. \quad (\text{D28})$$

We are now prepared to present numerical results obtained using the perturbation approach. The neglect of  $G^{(\text{sp})}$  and  $G^{(\text{pp})}$  corresponds to the spin-phonon model presented in Appendix B, which can be solved exactly.

Consequently, we can utilize the exact solution as a benchmark to evaluate the accuracy of the perturbation approach, and we choose bulk CrI<sub>3</sub> as the benchmark system. In Table XII we provide several quantities calculated using perturbed energies and states. These include the second-order-perturbed phonon energies, the first-order-perturbed phonon states represented by the coefficients  $c_{\nu n}^{(1)}$  defined in Eq. (D13), and the second-order-perturbed magnon energies. The corresponding exact results are also included in Table XII for benchmarking purposes, and we find that the perturbation treatment reproduces the exact solutions to very good accuracy. We have performed calculations of the angular momentum  $L_z$  using the second-order-perturbed phonon states, and the values obtained agree with the numbers presented in Table I up to the fourth decimal place. As a result, we do not include the specific numerical results for  $L_z$  explicitly in the Table.

## 2. Perturbation treatment of $G^{(\text{sp})}$

The treatment of  $G^{(\text{sp})}$  in the perturbation framework follows a similar procedure as that of  $K^{(\text{sp})}$ . In this case, we neglect  $K^{(\text{sp})}$  and  $G^{(\text{pp})}$ . Since  $G^{(\text{sp})}$  is block off-diagonal, the first-order perturbation of the energy is also zero. By substituting  $K^{(\text{sp})}$  with  $i\omega_n G^{(\text{sp})}$  in Eq. (D16), we can obtain  $|u_n^{(1)}\rangle$  due to  $G^{(\text{sp})}$ . Similarly, perturbations  $\omega_n^{(2)}$  and  $|u_n^{(2)}\rangle$  due to  $G^{(\text{sp})}$  can be obtained by replacing  $K^{(\text{sp})}$  with  $i\omega_n G^{(\text{sp})}$  in Eqs. (D20) and (D22) respectively. Perturbations of magnons can be obtained in the same manner.

## 3. Perturbation treatment of $G^{(\text{pp})}$

In this section we explore the perturbation treatment of  $G^{(\text{pp})}$ , this time neglecting  $K^{(\text{sp})}$  and  $G^{(\text{sp})}$ . Taking the perturbation to be  $\lambda G^{(\text{pp})}$ , Eq. (D1) simplifies to

$$(K^{(\text{pp})} + i\omega_n G^{(\text{pp})} - \xi_n M^{(\text{pp})})|u_n\rangle = 0. \quad (\text{D29})$$

We expand each term as

$$\begin{aligned} \omega_n &= \omega_n^{(0)} + \lambda\omega_n^{(1)} + \lambda^2\omega_n^{(2)} + \dots, \\ \xi_n &= \xi_n^{(0)} + \lambda\xi_n^{(1)} + \lambda^2\xi_n^{(2)} + \dots, \\ |u_n\rangle &= |u_n^{(0)}\rangle + \lambda|u_n^{(1)}\rangle + \lambda^2|u_n^{(2)}\rangle + \dots, \end{aligned} \quad (\text{D30})$$

where  $K^{(\text{pp})}$  and  $M^{(\text{pp})}$  are of zeroth order in  $\lambda$ , and  $G^{(\text{pp})}$  is of first order in  $\lambda$ .

Expanding Eq. (D29) to the first order in  $\lambda$ , we obtain

$$\begin{aligned} (K^{(\text{pp})} - \xi_n^{(0)} M^{(\text{pp})})|u_n^{(1)}\rangle \\ + (i\omega_n^{(0)} G^{(\text{pp})} - \xi_n^{(1)} M^{(\text{pp})})|u_n^{(0)}\rangle = 0. \end{aligned} \quad (\text{D31})$$

Multiplying Eq. (D31) by  $\langle u_n^{(0)}|$  from the left, we find the first-order perturbation to the phonon energy as

$$\begin{aligned} \xi_n^{(1)} &= \omega_n^{(0)} \langle u_n^{(0)} | iG^{(\text{pp})} | u_n^{(0)} \rangle, \\ \omega_n^{(1)} &= \frac{1}{2} \langle u_n^{(0)} | iG^{(\text{pp})} | u_n^{(0)} \rangle. \end{aligned} \quad (\text{D32})$$

Multiplying Eq. (D31) by  $\langle u_m^{(0)}|$  from the left, we obtain the first-order perturbation to  $|u_n\rangle$  as

$$|u_n^{(1)}\rangle = \sum_{m \neq n} \frac{i\omega_n \langle u_m^{(0)} | G^{(\text{pp})} | u_n^{(0)} \rangle}{\xi_n^{(0)} - \xi_m^{(0)}} |u_m^{(0)}\rangle. \quad (\text{D33})$$

Since the first-order perturbations to energies and phonon states are non-zero in this case, we do not go beyond first order here, although generalizing to higher orders is straightforward.

- 
- [1] Xavier Gonze and Changyol Lee, “Dynamical matrices, Born effective charges, dielectric permittivity tensors, and interatomic force constants from density-functional perturbation theory,” *Phys. Rev. B* **55**, 10355–10368 (1997).
- [2] Stefano Baroni, Stefano de Gironcoli, Andrea Dal Corso, and Paolo Giannozzi, “Phonons and related crystal properties from density-functional perturbation theory,” *Rev. Mod. Phys.* **73**, 515–562 (2001).
- [3] Atsushi Togo, Laurent Chaput, Terumasa Tadano, and Isao Tanaka, “Implementation strategies in phonopy and phono3py,” *J. Phys. Condens. Matter* **35**, 353001 (2023).
- [4] Feliciano Giustino, “Electron-phonon interactions from first principles,” *Rev. Mod. Phys.* **89**, 015003 (2017).
- [5] Bartomeu Monserrat, “Electron-phonon coupling from finite differences,” *Journal of Physics: Condensed Matter* **30**, 083001 (2018).
- [6] A.I. Liechtenstein, M.I. Katsnelson, V.P. Antropov, and V.A. Gubanov, “Local spin density functional approach to the theory of exchange interactions in ferromagnetic metals and alloys,” *Journal of Magnetism and Magnetic Materials* **67**, 65–74 (1987).
- [7] S. V. Halilov, H. Eschrig, A. Y. Perlov, and P. M. Oppeneer, “Adiabatic spin dynamics from spin-density-functional theory: Application to Fe, Co, and Ni,” *Phys. Rev. B* **58**, 293–302 (1998).
- [8] Liqin Ke and Mikhail I. Katsnelson, “Electron correlation effects on exchange interactions and spin excitations in 2d van der Waals materials,” *npj Computational Materials* **7**, 4 (2021).
- [9] Frederik L Durhuus, Thorbjørn Skovhus, and Thomas Olsen, “Plane wave implementation of the magnetic force

- theorem for magnetic exchange constants: application to bulk Fe, Co and Ni,” *Journal of Physics: Condensed Matter* **35**, 105802 (2023).
- [10] S. Y. Savrasov, “Linear response calculations of spin fluctuations,” *Phys. Rev. Lett.* **81**, 2570–2573 (1998).
- [11] S. Lounis, A. T. Costa, R. B. Muniz, and D. L. Mills, “Theory of local dynamical magnetic susceptibilities from the Korringa-Kohn-Rostoker Green function method,” *Phys. Rev. B* **83**, 035109 (2011).
- [12] Bruno Rousseau, Asier Eiguren, and Aitor Bergara, “Efficient computation of magnon dispersions within time-dependent density functional theory using maximally localized Wannier functions,” *Phys. Rev. B* **85**, 054305 (2012).
- [13] A. L. Wysocki, V. N. Valmispild, A. Kutepov, S. Sharma, J. K. Dewhurst, E. K. U. Gross, A. I. Lichtenstein, and V. P. Antropov, “Spin-density fluctuations and the fluctuation-dissipation theorem in 3d ferromagnetic metals,” *Phys. Rev. B* **96**, 184418 (2017).
- [14] Kun Cao, Henry Lambert, Paolo G. Radaelli, and Feliciano Giustino, “Ab initio calculation of spin fluctuation spectra using time-dependent density functional perturbation theory, plane waves, and pseudopotentials,” *Phys. Rev. B* **97**, 024420 (2018).
- [15] N. Tancogne-Dejean, F. G. Eich, and A. Rubio, “Time-dependent magnons from first principles,” *Journal of Chemical Theory and Computation* **16**, 1007–1017 (2020), pMID: 31922758.
- [16] Thorbjørn Skovhus and Thomas Olsen, “Dynamic transverse magnetic susceptibility in the projector augmented-wave method: Application to Fe, Ni, and Co,” *Phys. Rev. B* **103**, 245110 (2021).
- [17] Tommaso Gorni, Oscar Baseggio, Pietro Delugas, Stefano Baroni, and Iurii Timrov, “turbomagnon – a code for the simulation of spin-wave spectra using the Liouville-Lanczos approach to time-dependent density-functional perturbation theory,” *Computer Physics Communications* **280**, 108500 (2022).
- [18] F. Aryasetiawan and K. Karlsson, “Green’s function formalism for calculating spin-wave spectra,” *Phys. Rev. B* **60**, 7419–7428 (1999).
- [19] K. Karlsson and F. Aryasetiawan, “Spin-wave excitation spectra of nickel and iron,” *Phys. Rev. B* **62**, 3006–3009 (2000).
- [20] Takao Kotani and Mark van Schilfhaarde, “Spin wave dispersion based on the quasiparticle self-consistent GW method: NiO, MnO and  $\alpha$ -MnAs,” *Journal of Physics: Condensed Matter* **20**, 295214 (2008).
- [21] Ersoy Şaşıoğlu, Arno Schindlmayr, Christoph Friedrich, Frank Freimuth, and Stefan Blügel, “Wannier-function approach to spin excitations in solids,” *Phys. Rev. B* **81**, 054434 (2010).
- [22] Mathias C. T. D. Müller, Stefan Blügel, and Christoph Friedrich, “Electron-magnon scattering in elementary ferromagnets from first principles: Lifetime broadening and band anomalies,” *Phys. Rev. B* **100**, 045130 (2019).
- [23] Pietro Delugas, Oscar Baseggio, Iurii Timrov, Stefano Baroni, and Tommaso Gorni, “Magnon-phonon interactions enhance the gap at the Dirac point in the spin-wave spectra of CrI<sub>3</sub> two-dimensional magnets,” *Phys. Rev. B* **107**, 214452 (2023).
- [24] Max Born and Kun Huang, *Dynamical Theory of Crystal Lattices*, International Series of Monographs on Physics (Oxford University Press, Walton Street, Oxford OX2 6DP, UK, 1954).
- [25] C. Alden Mead and Donald G. Truhlar, “On the determination of Born–Oppenheimer nuclear motion wave functions including complications due to conical intersections and identical nuclei,” *The Journal of Chemical Physics* **70**, 2284–2296 (1979).
- [26] Lifa Zhang and Qian Niu, “Angular momentum of phonons and the Einstein–de Haas effect,” *Phys. Rev. Lett.* **112**, 085503 (2014).
- [27] Hao Chen, Wei Zhang, Qian Niu, and Lifa Zhang, “Chiral phonons in two-dimensional materials,” *2D Materials* **6**, 012002 (2018).
- [28] Sinisa Coh, “Classification of materials with phonon angular momentum and microscopic origin of angular momentum,” (2021), [arXiv:1911.05064 \[cond-mat.mtrl-sci\]](https://arxiv.org/abs/1911.05064).
- [29] Hisayoshi Komiyama and Shuichi Murakami, “Universal features of canonical phonon angular momentum without time-reversal symmetry,” *Phys. Rev. B* **103**, 214302 (2021).
- [30] Oliviero Bistoni, Francesco Mauri, and Matteo Calandra, “Intrinsic vibrational angular momentum from nonadiabatic effects in noncollinear magnetic molecules,” *Phys. Rev. Lett.* **126**, 225703 (2021).
- [31] Daniyar Saparov, Bangguo Xiong, Yafei Ren, and Qian Niu, “Lattice dynamics with molecular Berry curvature: Chiral optical phonons,” *Phys. Rev. B* **105**, 064303 (2022).
- [32] Qianqian Wang, Si Li, Jiaojiao Zhu, Hao Chen, Weikang Wu, Weibo Gao, Lifa Zhang, and Shengyuan A. Yang, “Chiral phonons in lattices with  $C_4$  symmetry,” *Phys. Rev. B* **105**, 104301 (2022).
- [33] John Bonini, Shang Ren, David Vanderbilt, Massimiliano Stengel, Cyrus E. Dreyer, and Sinisa Coh, “Frequency splitting of chiral phonons from broken time-reversal symmetry in CrI<sub>3</sub>,” *Phys. Rev. Lett.* **130**, 086701 (2023).
- [34] Lifa Zhang, Jie Ren, Jian-Sheng Wang, and Baowen Li, “Topological nature of the phonon Hall effect,” *Phys. Rev. Lett.* **105**, 225901 (2010).
- [35] Tao Qin, Jianhui Zhou, and Junren Shi, “Berry curvature and the phonon Hall effect,” *Phys. Rev. B* **86**, 104305 (2012).
- [36] Lifa Zhang, “Berry curvature and various thermal Hall effects,” *New Journal of Physics* **18**, 103039 (2016).
- [37] Takuma Saito, Kou Misaki, Hiroaki Ishizuka, and Naoto Nagaosa, “Berry phase of phonons and thermal Hall effect in nonmagnetic insulators,” *Phys. Rev. Lett.* **123**, 255901 (2019).
- [38] Luojun Du, Jian Tang, Yanchong Zhao, Xiaomei Li, Rong Yang, Xuerong Hu, Xueyin Bai, Xiao Wang, Kenji Watanabe, Takashi Taniguchi, Dongxia Shi, Guoqiang Yu, Xuedong Bai, Tawfique Hasan, Guangyu Zhang, and Zhipei Sun, “Lattice dynamics, phonon chirality, and spin–phonon coupling in 2D itinerant ferromagnet Fe<sub>3</sub>GeTe<sub>2</sub>,” *Advanced Functional Materials* **29**, 1904734 (2019).
- [39] Tingting Yin, Kanchan Ajit Ulman, Sheng Liu, Andrés Granados del Águila, Yuqing Huang, Lifa Zhang, Marco Serra, David Sedmidubsky, Zdenek Sofer, Su Ying Quek, and Qihua Xiong, “Chiral phonons and giant magneto-optical effect in CrBr<sub>3</sub> 2D magnet,” *Advanced Materials* **33**, 2101618 (2021).
- [40] G. Grissonnanche, A. Legros, S. Badoux, E. Lefrançois,

- V. Zlatko, M. Lizaire, F. Laliberté, A. Gourgout, J. S. Zhou, S. Pyon, T. Takayama, H. Takagi, S. Ono, N. Doiron-Leyraud, and L. Taillefer, “Giant thermal Hall conductivity in the pseudogap phase of cuprate superconductors,” *Nature* **571**, 376–380 (2019).
- [41] Heda Zhang, Chunqiang Xu, Caitlin Carnahan, Milos Sretenovic, Nishchay Suri, Di Xiao, and Xianglin Ke, “Anomalous thermal Hall effect in an insulating van der Waals magnet,” *Phys. Rev. Lett.* **127**, 247202 (2021).
- [42] Shao-Yu Chen, Changxi Zheng, Michael S. Fuhrer, and Jun Yan, “Helicity-resolved Raman scattering of MoS<sub>2</sub>, MoSe<sub>2</sub>, WS<sub>2</sub>, and WSe<sub>2</sub> atomic layers,” *Nano Letters* **15**, 2526–2532 (2015), pMID: 25719859.
- [43] Xiaotong Chen, Xin Lu, Sudipta Dubey, Qiang Yao, Sheng Liu, Xingzhi Wang, Qihua Xiong, Lifa Zhang, and Ajit Srivastava, “Entanglement of single-photons and chiral phonons in atomically thin WSe<sub>2</sub>,” *Nature Physics* **15**, 221–227 (2019).
- [44] Hanyu Zhu, Jun Yi, Ming-Yang Li, Jun Xiao, Lifa Zhang, Chih-Wen Yang, Robert A. Kaindl, Lain-Jong Li, Yuan Wang, and Xiang Zhang, “Observation of chiral phonons,” *Science* **359**, 579–582 (2018).
- [45] Lifa Zhang and Qian Niu, “Chiral phonons at high-symmetry points in monolayer hexagonal lattices,” *Phys. Rev. Lett.* **115**, 115502 (2015).
- [46] Hannes Hübener, Umberto De Giovannini, and Angel Rubio, “Phonon driven Floquet matter,” *Nano Letters* **18**, 1535–1542 (2018), pMID: 29361223.
- [47] Yafei Ren, Cong Xiao, Daniyar Saparov, and Qian Niu, “Phonon magnetic moment from electronic topological magnetization,” *Phys. Rev. Lett.* **127**, 186403 (2021).
- [48] Dominik M. Juraschek, Tomáš Neuman, and Prineha Narang, “Giant effective magnetic fields from optically driven chiral phonons in 4f paramagnets,” *Phys. Rev. Res.* **4**, 013129 (2022).
- [49] Xiao-Wei Zhang, Yafei Ren, Chong Wang, Ting Cao, and Di Xiao, “Gate-tunable phonon magnetic moment in bilayer graphene,” *Phys. Rev. Lett.* **130**, 226302 (2023).
- [50] Qian Niu and Leonard Kleinman, “Spin-wave dynamics in real crystals,” *Phys. Rev. Lett.* **80**, 2205–2208 (1998).
- [51] Ralph Gebauer and Stefano Baroni, “Magnons in real materials from density-functional theory,” *Phys. Rev. B* **61**, R6459–R6462 (2000).
- [52] Lev Davidovich Landau and E Lifshitz, “On the theory of the dispersion of magnetic permeability in ferromagnetic bodies,” *Phys. Z. Sowjet.* **8**, 153 (1935).
- [53] Q. Niu, Xindong Wang, L. Kleinman, Wu-Ming Liu, D. M. C. Nicholson, and G. M. Stocks, “Adiabatic dynamics of local spin moments in itinerant magnets,” *Phys. Rev. Lett.* **83**, 207–210 (1999).
- [54] David Vanderbilt, *Berry Phases in Electronic Structure Theory: Electric Polarization, Orbital Magnetization and Topological Insulators* (Cambridge University Press, 2018) Chap. 3.
- [55] G. Kresse and J. Hafner, “Ab initio molecular dynamics for liquid metals,” *Phys. Rev. B* **47**, 558–561 (1993).
- [56] G. Kresse and J. Furthmüller, “Efficient iterative schemes for ab initio total-energy calculations using a plane-wave basis set,” *Phys. Rev. B* **54**, 11169–11186 (1996).
- [57] G. Kresse and D. Joubert, “From ultrasoft pseudopotentials to the projector augmented-wave method,” *Phys. Rev. B* **59**, 1758–1775 (1999).
- [58] J. P. Perdew and Alex Zunger, “Self-interaction correction to density-functional approximations for many-electron systems,” *Phys. Rev. B* **23**, 5048–5079 (1981).
- [59] P. E. Blöchl, “Projector augmented-wave method,” *Phys. Rev. B* **50**, 17953–17979 (1994).
- [60] Hendrik J. Monkhorst and James D. Pack, “Special points for Brillouin-zone integrations,” *Phys. Rev. B* **13**, 5188–5192 (1976).
- [61] S. L. Dudarev, G. A. Botton, S. Y. Savrasov, C. J. Humphreys, and A. P. Sutton, “Electron-energy-loss spectra and the structural stability of nickel oxide: An LSDA+U study,” *Phys. Rev. B* **57**, 1505–1509 (1998).
- [62] Sai Mu and K. D. Belashchenko, “Influence of strain and chemical substitution on the magnetic anisotropy of antiferromagnetic Cr<sub>2</sub>O<sub>3</sub>: An ab-initio study,” *Phys. Rev. Mater.* **3**, 034405 (2019).
- [63] Bheema Lingam Chittari, Youngju Park, Dongkyu Lee, Moon-sup Han, Allan H. MacDonald, Euyheon Hwang, and Jeil Jung, “Electronic and magnetic properties of single-layer MPX<sub>3</sub> metal phosphorous trichalcogenides,” *Phys. Rev. B* **94**, 184428 (2016).
- [64] Mark E. Turiansky, Audrius Alkauskas, Manuel Engel, Georg Kresse, Darshana Wickramaratne, Jimmy-Xuan Shen, Cyrus E. Dreyer, and Chris G. Van de Walle, “Nonrad: Computing nonradiative capture coefficients from first principles,” *Computer Physics Communications* **267**, 108056 (2021).
- [65] Harold T. Stokes and Dorian M. Hatch, “*FINDSYM*: program for identifying the space-group symmetry of a crystal,” *Journal of Applied Crystallography* **38**, 237–238 (2005).
- [66] Atsushi Togo and Isao Tanaka, “*Spglib*: a software library for crystal symmetry search,” (2018), [arXiv:1808.01590 \[cond-mat.mtrl-sci\]](https://arxiv.org/abs/1808.01590).
- [67] Koichi Momma and Fujio Izumi, “*VESTA3* for three-dimensional visualization of crystal, volumetric and morphology data,” *Journal of Applied Crystallography* **44**, 1272–1276 (2011).
- [68] Bevin Huang, Genevieve Clark, Efrén Navarro-Moratalla, Dahlia R. Klein, Ran Cheng, Kyle L. Seyler, Ding Zhong, Emma Schmidgall, Michael A. McGuire, David H. Cobden, Wang Yao, Di Xiao, Pablo Jarillo-Herrero, and Xiaodong Xu, “Layer-dependent ferromagnetism in a van der Waals crystal down to the monolayer limit,” *Nature* **546**, 270–273 (2017).
- [69] Mildred S Dresselhaus, Gene Dresselhaus, and Ado Jorio, *Group theory: application to the physics of condensed matter* (Springer Science & Business Media, 2007).
- [70] Shangfei Wu, Kai Du, Sang-Wook Cheong, and Girsh Blumberg, “unpublished.”
- [71] Mois Iia Aroyo, Juan Manuel Perez-Mato, Cesar Capillas, Eli Kroumova, Svetoslav Ivantchev, Gotzon Madariaga, Asen Kirov, and Hans Wondratschek, “Bilbao Crystallographic Server: I. Databases and crystallographic computing programs,” *Zeitschrift für Kristallographie - Crystalline Materials* **221**, 15–27 (2006).
- [72] Mois I. Aroyo, Asen Kirov, Cesar Capillas, J. M. Perez-Mato, and Hans Wondratschek, “Bilbao Crystallographic Server. II. Representations of crystallographic point groups and space groups,” *Acta Crystallographica Section A* **62**, 115–128 (2006).
- [73] M.I. Aroyo, J.M. Perez-Mato, D. Orobengoa, E. Tasci, G. De La Flor, and A. Kirov, “Crystallography online: Bilbao crystallographic server,” *Bulgarian Chemical Communications* **43**, 183 – 197 (2011).
- [74] Samuel V. Gallego, Emre S. Tasci, Gemma de la Flor,



- J. Manuel Perez-Mato, and Mois I. Aroyo, “Magnetic symmetry in the Bilbao Crystallographic Server: a computer program to provide systematic absences of magnetic neutron diffraction,” *Journal of Applied Crystallography* **45**, 1236–1247 (2012).
- [75] Nikhil Sivadas, Satoshi Okamoto, Xiaodong Xu, Craig J. Fennie, and Di Xiao, “Stacking-dependent magnetism in bilayer CrI<sub>3</sub>,” *Nano Letters* **18**, 7658–7664 (2018), pMID: 30408960.
- [76] Vijay Kumar Gudelli and Guang-Yu Guo, “Magnetism and magneto-optical effects in bulk and few-layer CrI<sub>3</sub>: a theoretical GGA + U study,” *New Journal of Physics* **21**, 053012 (2019).
- [77] John P. Perdew, Kieron Burke, and Matthias Ernzerhof, “Generalized gradient approximation made simple,” *Phys. Rev. Lett.* **77**, 3865–3868 (1996).
- [78] Sándor Tóth, Björn Wehinger, Katharina Rolfs, Turan Birol, Uwe Stuhr, Hiroshi Takatsu, Kenta Kimura, Tsuyoshi Kimura, Henrik M Rønnow, and Christian Rüegg, “Electromagnon dispersion probed by inelastic x-ray scattering in licro2,” *Nature communications* **7**, 13547 (2016).
- [79] P. Padmanabhan, F. L. Buessen, R. Tutchton, K. W. C. Kwock, S. Gilinsky, M. C. Lee, M. A. McGuire, S. R. Singamaneni, D. A. Yarotski, A. Paramakanti, J. X. Zhu, and R. P. Prasankumar, “Coherent helicity-dependent spin-phonon oscillations in the ferromagnetic van der Waals crystal CrI<sub>3</sub>,” *Nature Communications* **13**, 4473 (2022).
- [80] Igor Mazin (The PRX Editors), “Editorial: Altermagnetism—a new punch line of fundamental magnetism,” *Phys. Rev. X* **12**, 040002 (2022).
- [81] Libor Šmejkal, Jairo Sinova, and Tomas Jungwirth, “Emerging research landscape of altermagnetism,” *Phys. Rev. X* **12**, 040501 (2022).
- [82] Giuseppe Grosso and Giuseppe Pastori Parravicini, *Solid State Physics* (Academic press, 2013).